

Magnetization Dependent In-plane Anomalous Hall Effect in a Low-dimensional System

I-Hsuan Kao^{1†}, Ravi Kumar Bandapelli^{1†}, Zhenhong Cui¹, Shuchen Zhang¹, Jian Tang², Tiema Qian³, Souvik Sasmal¹, Aalok Tiwari¹, Mei-Tung Chen¹, Rahul Rao⁴, Jiahua Li⁵, James H. Edgar⁵, Kenji Watanabe⁶, Takashi Taniguchi⁷, Ni Ni³, Su-Yang Xu⁸, Qiong Ma², Shubhayu Chatterjee¹, Jyoti Katoch¹, Simranjeet Singh^{1*}

¹Department of Physics, Carnegie Mellon University, Pittsburgh, 15213, PA, USA.

²Department of Physics, Boston College, Chestnut Hill, 02467, MA, USA.

³Department of Physics and Astronomy and the California NanoSystems Institute, University of California, Los Angeles, 90095, CA, USA.

⁴Materials and Manufacturing Directorate, Air Force Research Laboratory, Dayton, 45433, OH, USA.

⁵Tim Taylor Department of Chemical Engineering, Kansas State University, Manhattan, 66506, KS, USA.

⁶Research Center for Electronic and Optical Materials, National Institute for Materials Science, Tsukuba, 305-0044, Japan.

⁷Research Center for Materials Nanoarchitectonics, National Institute for Materials Science, Tsukuba, 305-0044, Japan.

⁸Department of Chemistry and Chemical Biology, Harvard University, Cambridge, 02138, MA, USA.

*Email: simranjs@andrew.cmu.edu ;

†These authors contributed equally to this work.

Abstract

Anomalous Hall Effect (AHE) response in magnetic systems is typically proportional to an out-of-plane magnetization component because of the restriction imposed by system symmetries, which demands that the magnetization, applied electric field, and induced Hall current are mutually orthogonal to each other. Here, we report experimental realization of an unconventional form of AHE in a low-dimensional heterostructure, wherein the Hall response is not only proportional to the out-of-plane magnetization component but also to the in-plane magnetization component. By interfacing a low-symmetry topological semimetal (TaIrTe₄) with the ferromagnetic insulator (Cr₂Ge₂Te₆), we create a low-dimensional magnetic system, where only one mirror symmetry is preserved. We show that as long as the magnetization has a finite component in the mirror plane, this last mirror symmetry is broken, allowing the emergence of an AHE signal proportional to in-plane magnetization. Our experiments, conducted on multiple devices, reveal a gate-voltage-dependent AHE response, suggesting that the underlying mechanisms responsible for the Hall effect in our system can be tuned via electrostatic gating. A minimal microscopic model constrained by the symmetry of the heterostructure shows that both interfacial spin-orbit coupling and time-reversal symmetry breaking via the exchange interaction from magnetization are responsible for the emergence of the in-plane AHE. Our work highlights the importance of system symmetries and exchange interaction in low-dimensional heterostructures for designing novel and tunable Hall effects in layered quantum systems.

Introduction

The Anomalous Hall effect (AHE) is intrinsically associated with the Berry-phase and has played an important role in probing magnetism and other quantum phenomena in solid-state systems [1, 2]. Conventionally, AHE in ferromagnets refers to magnetization-dependent Hall resistance, with the orientation of magnetization, applied electric field, and the Hall current being mutually orthogonal to each other. [3–6]. Therefore, the AHE and its quantized counterpart (quantum anomalous Hall effect, QAHE),

are typically associated with out-of-plane magnetization, i.e., the magnetization is perpendicular to the plane spanned by the applied electric field and Hall current. The prerequisite for AHE, i.e., time-reversal (\mathcal{T}) symmetry breaking, does not put a constraint on the orientation of the magnetization, instead, the orthogonality restriction in conventional AHE is rooted in material system's rotational and/or mirror symmetries [7, 8]. Unconventional AHE, wherein the Hall resistance is proportional

to in-plane magnetization, has been theoretically predicted in magnetic systems with lower crystal symmetry [7–14]. Experimentally, unconventional Hall effects driven by in-plane magnetization and/or magnetic field have been reported in limited three-dimensional (3D) systems, including the kagome ferromagnet [10, 15], magnetic Weyl semimetal [16, 17], topological semimetals where Berry curvature is generated by band topology [18–20], and magnetic octupole in Fe and Ni films [21]. In addition, an in-plane AHE has been reported in a heterodimensional superlattice VS₂/VS; however, it is primarily attributed to Berry curvature generated by the interplay between spin-orbit coupling (SOC) and an in-plane magnetic field, rather than arising from an in-plane magnetization due to ferromagnetic ordering [22]. To date, the experimental realization of an in-plane magnetization-induced AHE in a two-dimensional (2D) system, which can provide a pathway for achieving QAHE in an in-plane magnetic configuration to expand the parameter space for designing dissipationless edge transport in low-dimensional systems [11, 12], remains notably missing.

Here, we report the experimental realization of an unconventional AHE, associated with both out-of-plane and in-plane magnetization, in a 2D topological system. To achieve this, we engineer a low-symmetry magnetic heterostructure by combining a low-symmetry topological semimetal, TaIrTe₄, with a layered ferromagnetic insulator, Cr₂Ge₂Te₆ (CGT), which is particularly suited for hosting unconventional AHE. We demonstrate that the observed Hall response in these heterostructures can be driven solely by the magnetization in CGT, even when it lies entirely in the plane. To elucidate the underlying mechanism, we develop a minimal microscopic model constrained by the symmetry of the heterostructure, showing that both interfacial spin-orbit coupling (SOC) and time-reversal symmetry breaking via the exchange interaction from magnetization are essential to the emergence of the in-plane AHE. Our findings establish the first experimental demonstration of a magnetization-driven in-plane AHE in a 2D heterostructure, and provide theoretical insight into the key ingredients necessary for realizing such unconventional Hall responses, potentially paving the way for their quantum counterparts in future studies.

Symmetry Constraints on Anomalous Hall Effect

We begin by illustrating the physical origin of unconventional in-plane AHE in 2D materials via symmetry considerations, which motivates our specific heterostructure choice. Such symmetry requirements for the emergence of unconventional AHE have been established for general 3D materials [7] — all rotational and mirror symmetries must be broken when the magnetization lies in-plane. An alternative strategy to engineer AHE in 2D is to build magnetic heterostructures with sufficiently low symmetry and intrinsic magnetic moments. Here, the magnetization is introduced via proximity to a magnetic material, and both the interface and the magnetization serve to reduce the symmetry as desired [23],

Any linear Hall effect, wherein the Hall voltage is proportional to the charge current, can only occur in the absence of a mirror symmetry with the reflection plane

parallel to the out-of-plane direction. To see this, consider the set-up shown schematically in Fig. 1a, where a charge current density J_a is applied along the a -axis and a perpendicular electric field E_b is generated due to the Hall effect. Under the action of a mirror \mathcal{M}_a , E_b remains unchanged while J_a reverses direction ($J_a \rightarrow -J_a$). However, an electric field induced by any linear Hall effect must reverse sign when the current density is reversed, enforcing the Hall resistivity $\rho_{ba} = E_b/J_a$ to be zero. By contrast, if the mirror symmetry \mathcal{M}_a is broken, either via the interface or the magnetization, then ρ_{ba} is generically non-zero.

Our intuitive picture can be put on a more formal footing by assuming an intrinsic origin of the AHE, wherein the Hall conductivity σ_{ab} is set by the integral of the Berry curvature $\Omega(\mathbf{k})$ over all occupied states in a band with dispersion $\varepsilon(\mathbf{k})$, i.e., $\sigma_{ab} \propto \int_{\mathbf{k}} \Omega(\mathbf{k}) n_F[\varepsilon(\mathbf{k})]$ [?]. As long as time-reversal symmetry \mathcal{T} is present, the Berry curvature is odd under \mathcal{T} , i.e., $\Omega(\mathbf{k}) = -\Omega(-\mathbf{k})$, while the dispersion is even, i.e., $\varepsilon(\mathbf{k}) = \varepsilon(-\mathbf{k})$, enforcing that σ_{ab} vanishes. If time-reversal symmetry is broken by magnetization \mathbf{m} , the Berry curvature $\Omega(\mathbf{k})$ can be non-zero. \mathbf{m} also plays a crucial role in mirror symmetry: being a pseudovector, it preserves (breaks) mirror symmetry when perpendicular (parallel) to the mirror plane (upper panel, Fig. 1b). Therefore, if \mathbf{m} is perpendicular to a mirror-plane for the heterostructure, say $\mathbf{m} \parallel \mathbf{a}$, then the mirror symmetry \mathcal{M}_a is preserved. Since the Berry curvature is a pseudoscalar in 2D, \mathcal{M}_a requires that the Berry curvature is odd in k_a , i.e., $\Omega(k_a, k_b) = -\Omega(-k_a, k_b)$, while the dispersion is even in k_a , i.e., $\varepsilon(k_a, k_b) = \varepsilon(-k_a, k_b)$, enforcing that the integral over k_a vanishes and thus $\sigma_{ab} = 0$. Consequently, one needs to construct a 2D heterostructure with a maximum of a single mirror plane, and arrange for the in-plane magnetization \mathbf{m} to have a component parallel to the said mirror plane, to observe an AHE.

To substantiate the above argument microscopically, we construct a minimal 2-band model by considering a 2D system with C_{2v} symmetry, that is reduced to C_s upon interfacing with a magnetic material (details in Methods and Fig. S8). The C_{2v} point group contains a two-fold rotational symmetry C_2 along the c -axis, as well as two mirror symmetries: $\mathcal{M}_a : (a, b, c) \rightarrow (-a, b, c)$, which corresponds to a mirror reflection with respect to the bc -plane, and $\mathcal{M}_b : (a, b, c) \rightarrow (a, -b, c)$, corresponding to a mirror reflection with respect to the ac -plane. Therefore, the simplest symmetry-allowed Hamiltonian, to quadratic order in momentum $\mathbf{k} = (k_a, k_b)$, is given by

$$H_0 = \frac{k_a^2}{2\tilde{m}_a} + \frac{k_b^2}{2\tilde{m}_b} + g_{ab}k_a s^b + g_{ba}k_b s^a \quad (1)$$

where $\mathbf{s} = (s_a, s_b, s_c)$ is the spin, \tilde{m}_a (\tilde{m}_b) is the effective mass along k_a (k_b), g_{ab} and g_{ba} are SOC constants. Without the presence of the magnetic interface, the C_2 and \mathcal{T} symmetries forbid any Berry curvature $\Omega(\mathbf{k})$, therefore, no intrinsic AHE is allowed.

Next, we consider the presence of a magnetic interface such that the C_{2v} point group is reduced to the C_s point group, where only one mirror symmetry \mathcal{M}_a is preserved. By considering the interfacial SOC and exchange interactions from magnetization, the Hamiltonian from Eq. 1 is

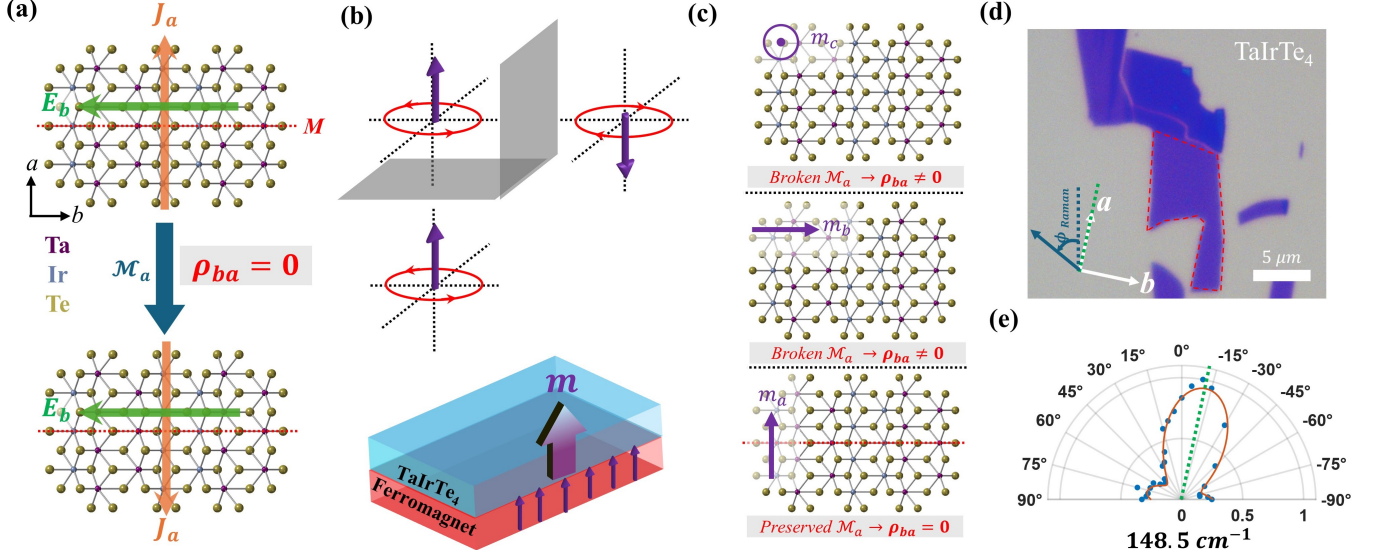


Fig. 1 Anomalous Hall effect and crystal symmetry. **a**, Visualization that AHE is not allowed in TaIrTe₄/CGT heterostructure, in C_s point group, when magnetic field (magnetization) is absent, as required by the \mathcal{M}_a symmetry. The \mathcal{M}_a symmetry operation reverses J_a but keeps E_b unchanged and, therefore, requires ρ_{ba} to be zero. **b**, Upper panel: Illustration showing that magnetization breaks mirror symmetries when their reflection planes are collinear with the magnetization direction, while it preserves those with reflection planes perpendicular to it. Lower panel: Demonstration that a low-symmetry magnetic heterostructure can be obtained by coupling a low-symmetry topological semimetal, TaIrTe₄, with a ferromagnet. **c**, Diagram showing that the AHE is only allowed when there is a finite magnetization component in the bc -plane of TaIrTe₄, which breaks the \mathcal{M}_a mirror symmetry. **d**, Optical image of a bilayer TaIrTe₄ flake used in device A, where the chosen region is outlined by the red dashed lines. The polarized Raman measurements were performed with the polarization of the incident laser oriented at an angle ϕ_{Raman} relative to the vertical direction. **e**, Angle-dependent polarized Raman spectral intensity at 148.5 cm^{-1} of TaIrTe₄ flake in **d**.

modified to

$$H = H_0 + g_{ac}k_a s^c + \tilde{g}_{ac}k_a^3 s^c - \Delta_{ex} \mathbf{m} \cdot \mathbf{s} \quad (2)$$

where g_{ac}, \tilde{g}_{ac} are two interfacial SOC constants that couple k_a and s_c , \mathbf{m} is the magnetization direction in the magnetic material, and Δ_{ex} is the exchange coupling strength. Note that g_{ab} and g_{ba} may be renormalized from their bare values in H_0 via interfacial SOC. When $\mathbf{m} \parallel \mathbf{a}$, the mirror-symmetry \mathcal{M}_a is preserved, therefore the intrinsic anomalous Hall conductivity calculated using the Hamiltonian in Eq. (2) vanishes. However, this constraint is lifted when there is finite magnetization in the bc -plane, which breaks the \mathcal{M}_a symmetry. In this case, we find a nonzero and asymmetric Berry curvature (Fig. S8e-f), and a resultant non-zero Hall conductance when $\mathbf{m} \parallel \mathbf{c}$ and $\mathbf{m} \parallel \mathbf{b}$ (see Fig. S8g). Thus, the reduced symmetries of our model allows it to exhibit AHE associated with both out-of-plane and in-plane magnetization. Notably, the additional SOC terms g_{ac}, \tilde{g}_{ac} , arising from broken C_2 symmetry, play a crucial role in enabling an asymmetric Berry curvature distribution $\Omega(\mathbf{k})$ when $m_b = \mathbf{m} \cdot \mathbf{b} \neq 0$, highlighting the importance of reduced symmetry for in-plane AHE in 2D heterostructures.

Motivated by our theoretical understanding, we purposefully construct a magnetic low-symmetry heterostructure that enables an AHE with in-plane magnetization. Specifically, we choose to interface few-layer TaIrTe₄ with a ferromagnet (FM), as illustrated in the lower panel of Fig. 1b. Bulk TaIrTe₄ is a type-II Weyl semimetal candidate that belongs to the C_{2v} point group and the Pmn2₁ space group [24, 25], while its monolayer has been identified as a quantum spin Hall insulator [26, 27]. In the TaIrTe₄/FM heterostructure, the interface reduces the symmetry to the C_s point group, preserving only a single

mirror symmetry \mathcal{M}_a , corresponding to reflection with respect to the bc -plane of TaIrTe₄. We select CGT as the FM layer due to its soft magnetic properties, which allow the magnetization to be aligned in any direction under a moderate magnetic field ($< 1 \text{ T}$) [28, 29]. Based on our formal theoretical considerations as well as the minimal microscopic model discussed above, the TaIrTe₄/CGT heterostructure should exhibit an AHE not only when the magnetization is out-of-plane, but also when it lies entirely in-plane.

The general form of AHE in TaIrTe₄/CGT heterostructure is summarized in Fig. 1c for three orthogonal magnetization configurations. When $\mathbf{m} \parallel \mathbf{c}$, all mirror symmetries with reflection planes along the c -axis, including \mathcal{M}_a , are broken, allowing an AHE response proportional to the magnetization component m_c . This also underscores why out-of-plane AHE is commonly observed in high-symmetry magnetic systems: the presence of multiple mirror symmetries with reflection planes along the z -axis, which can be simultaneously broken only by an out-of-plane magnetization. Since we focus on electric measurements in the ab -plane of TaIrTe₄, the c -axis corresponds to the out-of-plane (z -axis), making $m_z = m_c$. When $\mathbf{m} \parallel \mathbf{b}$, the mirror symmetry \mathcal{M}_a is also broken, leading to a unique, unconventional AHE term proportional to the in-plane magnetization m_b . Conversely, when $\mathbf{m} \parallel \mathbf{a}$, the mirror symmetry \mathcal{M}_a is preserved, forbidding any AHE contribution from m_a ($\rho_{ba} = 0$). Thus, the total AHE contribution to the Hall resistance R_{ba} in the TaIrTe₄/CGT heterostructure can be expressed as:

$$R_{ba} = \Delta R_{AHE}^z m_z + \Delta R_{AHE}^b m_b \quad (3)$$

where ΔR_{AHE}^z and ΔR_{AHE}^b are the AHE resistances associated with m_z and m_b , respectively.

We conclude this section by noting that Onsager reciprocal relations [30] constrain the Hall resistance to be anti-symmetric with respect to both the applied magnetic field \mathbf{B} and the magnetization \mathbf{m} in linear response, satisfying $R_{ba}(\mathbf{B}, \mathbf{m}) = R_{ab}(-\mathbf{B}, -\mathbf{m}) = -R_{ab}(\mathbf{B}, \mathbf{m})$. Therefore, R_{ba} can be extracted from the transverse resistance in the ab -plane of TaIrTe₄ measured under an arbitrary current direction via $R_{yx} = V_y/I_x = \frac{\sin(2\theta_I)}{2}(R_b - R_a) + R_{ba}$, where I_x is the applied current, V_y is the transverse voltage, θ_I is the angle between the current and the a -axis of TaIrTe₄, and R_a (R_b) is the longitudinal resistance along the a -axis (b -axis), with $R_b > R_a$ due to anisotropic resistivity [31, 32]. Notably, the antisymmetric Hall resistance $R_{ba} = -R_{ab}$ remains independent of the measurement orientation relative to the crystalline axes.

Device Fabrication and Characterization

For our experiments, we utilize atomically thin flakes of TaIrTe₄ (few-layer) and CGT (8-12 nm), and mechanical dry transfer and standard device fabrication techniques were used to assemble van der Waals (vdW) TaIrTe₄/CGT heterostructures and their devices [33, 34] (see Methods). We present experimental results from two devices, i.e., namely device A and device B. To investigate the unconventional AHE in TaIrTe₄/CGT heterostructures, it is crucial to identify the crystallographic orientation of TaIrTe₄ since the in-plane AHE has a unique in-plane magnetization dependence, which maximizes (vanishes) when $\mathbf{m} \parallel \mathbf{b}$ ($\mathbf{m} \parallel \mathbf{a}$). The optical image in Fig. 1d shows a bilayer TaIrTe₄ flake, where the outlined area is targeted for fabrication of device A. We characterized the crystallographic orientation by a combination of parallel cleaving edges and polarized Raman spectroscopy [27, 31, 35]. The normalized Raman intensity of TaIrTe₄ A₁ mode (at ~ 148.5 cm⁻¹) at each polarization angle (ϕ_{Raman}) relative to the vertical dashed line in Fig. 1d is plotted as a polar plot shown in Fig. 1e, depicting a period of 180° and the local intensity maxima occur along a - and b -axis. The A₁ mode shows Raman intensity maxima when the polarization is along the a -axis of TaIrTe₄ [27, 31, 35], therefore, the maximal intensity indicates the a -axis of TaIrTe₄ is 12° away from the vertical dashed blue line in Fig. 1d.

The optical micrograph of device A, composed of a bilayer TaIrTe₄ (Fig. 1d) and 11.9 nm CGT, is shown in Fig. 2a (upper panel) along with a side-view schematic of a typical device (lower panel). The flake thicknesses are confirmed by a combination of optical contrast and atomic force microscopy (AFM) (see Methods and Supplementary information). The polarized Raman spectra taken after the device fabrication (Fig. 1e) confirmed that the a -axis of TaIrTe₄ in device A is nearly aligned with the current channel of the Hall bar ($\sim 12^\circ$). We measure the electronic transport by lock-in amplifier techniques as illustrated in Fig. 2b, where a sinusoidal current $I = I_x \sin(\omega t)$ is applied while the in-phase first harmonic longitudinal (transverse) voltage response V_x (V_y) is measured. The current magnitude $I_x = 1 \mu\text{A}$ is used for all electric transport measurements for both Device A and B. In our devices, consisting of an atomically thin TaIrTe₄ layer and an insulating magnet, the electric transport in the TaIrTe₄ layer is tunable by applying an electrostatic

gate voltage (V_g), which adjusts the electron chemical potential in the TaIrTe₄ layer. The measured longitudinal resistance ($R_{xx} = V_x/I_x$) for device A as a function of V_g in a range of temperature from 11 K to 80 K is plotted in the upper panel of Fig. 2c. The line cuts at 11 K, 40 K, and 70 K in the lower panel of Fig. 2c show a clear resistance peak at the charge neutrality point (CNP). In the higher electron-doped (positive V_g) and hole-doped (negative V_g) regions, device A has metallic behavior, where the resistance monotonically decreases with decreasing temperatures. However, near the CNP at $V_g \sim 0$ V, a metal-insulator transition occurs around 60 K, as evident from the temperature dependence of R_{xx} measured at $V_g = 0$ V shown in Fig. 2d. The measured gate voltage and temperature dependence of R_{xx} are in good agreement with the measured electric transport of bilayer TaIrTe₄ [27].

Conventional Out-of-plane Anomalous Hall Effect

Next, we discuss the experimental observation of the conventional out-of-plane magnetization dependent AHE in device A, and the measurement setup is depicted in Fig. 2b. The transverse resistances presented in the main text are anti-symmetrized with respect to the magnetic field to isolate the Hall resistance (see Methods). We measured the Hall resistance as a function of the out-of-plane magnetic field B_z in device A at 11 K, as shown in Fig. 2e. Evidently, the Hall resistance contains contributions from both the ordinary Hall effect, arising from the applied field B_z , and the anomalous Hall effect, associated with the out-of-plane magnetization m_z in the CGT layer. The saturation observed in R_{yx} at $\pm B_z$ agrees well with the magnetic properties of CGT, i.e., the saturation magnetic field is around $B_z \sim 50$ mT with small coercivity at ~ 10 K [28, 29, 36, 37]. The saturated branches at high field (> 100 mT) were fitted using a linear function and a step function, with the step size defined as $2|\Delta R_{\text{AHE}}^z|$ (see Methods). The resistance component linear in the B -field, which is not associated with the magnetization, is removed, allowing us to isolate the anomalous Hall resistance ΔR_{AHE}^z .

This measurement of the AHE hysteresis loop was repeated at various temperatures, and the extracted ΔR_{AHE}^z is plotted as a function of temperature in Fig. 2f. The AHE signal vanishes near the Curie temperature of CGT (~ 61 K), indicating that the observed AHE in TaIrTe₄ arises from the magnetism in CGT layer [28, 29, 38]. This confirms the prediction of our theoretical model: the combination of interface-induced SOC and time-reversal symmetry breaking via exchange coupling to the magnetization in CGT gives rise to an asymmetric Berry curvature distribution in TaIrTe₄, resulting in a nonzero AHE response. [34, 39–45].

The observed AHE in device A is gate tunable by changing the electron chemical potential in TaIrTe₄ through electrostatic gating. To examine the gate tunability of AHE, we measured the R_{yx} vs B_z hysteresis loops at various V_g and is plotted in Fig. 2g. The extracted ΔR_{AHE}^z as a function of V_g in Fig. 2h shows a peak slightly away from the CNP, while the value is suppressed at higher $\pm V_g$. This experimental observation shows that

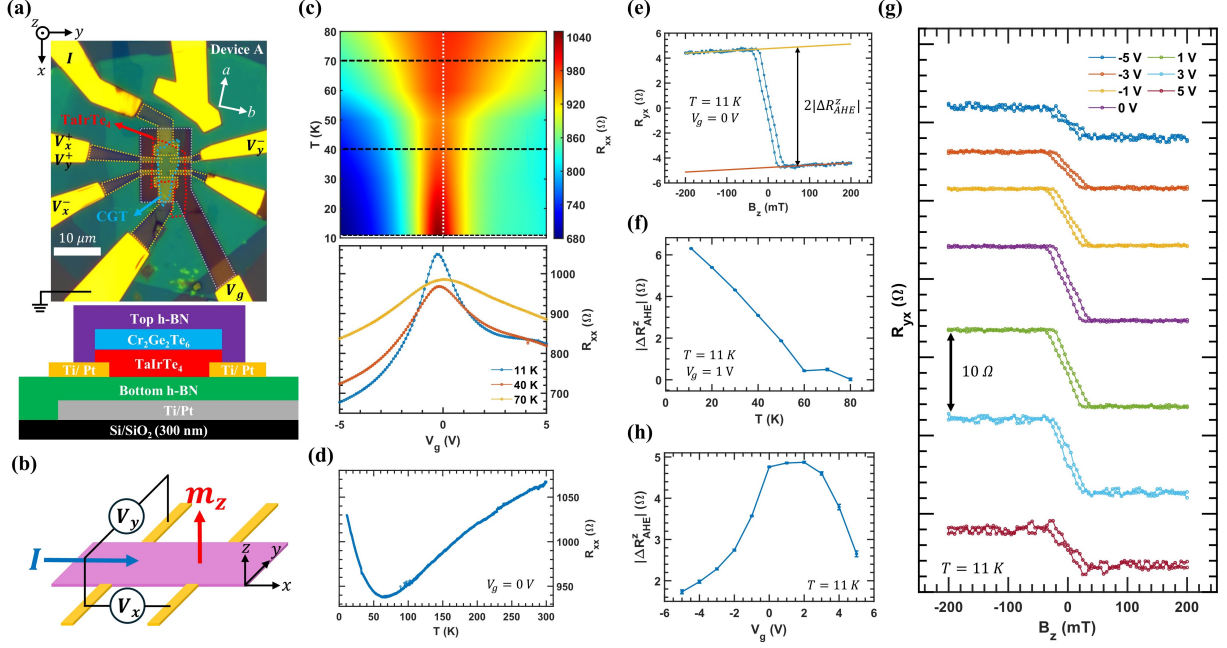


Fig. 2 Out-of-plane magnetization induced AHE in TaIrTe₄/CGT system. **a**, Upper panel: Optical image of device A with the a -axis of TaIrTe₄ aligned close to the current electrodes (about 12° tilted), with CGT, TaIrTe₄, and h-BN flakes outlined and labeled. The Pt electrodes (bottom gate) are outlined with dashed yellow (grey) lines. Lower panel: Schematic of the side view of a typical device. **b**, Schematic showing the configuration for the longitudinal and transverse resistance measurements with the magnetization oriented in the out-of-plane direction. **c**, Upper panel: Surface map of the measured longitudinal resistance (R_{xx}) of Device A as a function of gate voltage (V_g), for a range of temperatures (T). Lower panel: The R_{xx} vs V_g of Device A at 11 K, 40 K, and 70 K, as indicated by the black dashed lines in the surface map. **d**, The measured R_{xx} of device A as a function of temperature of at $V_g = 0$ V. **e**, The R_{yx} vs B_z hysteresis loop with the resistance offset removed. **f**, The measured m_z -dependent AHE resistance, ΔR_{AHE}^z , as a function of temperature at $V_g = 1$ V. **g**, The R_{yx} vs B_z hysteresis loops at 11 K in a range of V_g . **h**, ΔR_{AHE}^z as a function of V_g at 11 K.

the anomalous Hall resistance is sensitive to variations in the electron chemical potential, consistent with our theoretical expectations (Fig. S8g).

Unconventional In-plane Anomalous Hall Effect

To identify the unconventional AHE driven by in-plane magnetization, we leverage the weak magnetic anisotropy of CGT to control the direction of its magnetization \mathbf{m} using an external magnetic field. Since the magnetization of CGT can be easily saturated in any direction with a moderate field ($B > 300$ mT), this allows us to systematically probe the angular dependence of the AHE. We performed the R_{yx} vs B hysteresis loop measurements with the B -field aligned at different zy -plane rotation angles (γ_B), as illustrated in Fig. 3a. Based on Eq. 3, $\Delta R_{AHE}(\gamma_B)$ can be written as:

$$\Delta R_{AHE}(\gamma_B) = \Delta R_{AHE}^z \cos(\gamma_B) + \Delta R_{AHE}^y \sin(\gamma_B) \quad (4)$$

where $\Delta R_{AHE}^y = \sin(\alpha_b) \Delta R_{AHE}^b$ is the m_y -dependent AHE resistance. The additional factor of $\sin(\alpha_b)$ accounts for the slight misalignment between the TaIrTe₄ crystal axis and the electrodes, where α_b is the angle between the b -axis and the current channel (x -direction). The polarized Raman results determine $\alpha_b \sim 78^\circ$ in device A, however, with such a small misalignment, the measured ΔR_{AHE}^y is almost equivalent to ΔR_{AHE}^b with $\sin(\alpha_b) \sim 1$.

In Fig. 3b, the hysteresis loops measured with different γ_B at 0° ($\mathbf{B} \parallel \mathbf{z}$), 45°, 90° ($\mathbf{B} \parallel \mathbf{y}$), and 135° show clear signatures of unconventional in-plane AHE when $\mathbf{m} \parallel \mathbf{y}$. In our measurement setup in device A, we found $\Delta R_{AHE}^z (< 0)$ and $\Delta R_{AHE}^y (> 0)$ have opposite signs.

Due to the presence of a large in-plane AHE resistance, the addition (subtraction) of out-of-plane and in-plane AHE results in a larger (smaller) total AHE resistance magnitude at $\gamma_B = 135^\circ$ ($\gamma_B = 45^\circ$). Note that the presence of small peaks with γ_B at 45° and 135° is likely due to the PMA in CGT, thus, the magnetization first aligns partially along the out-of-plane direction at smaller B -fields when the magnetic field is tilted away from the plane. We repeated the hysteresis loop measurements in a range of γ_B (from -15° to 195°) and obtained the total AHE resistance ΔR_{AHE} as a function of γ_B (Fig. 3c). The measured γ_B dependence of ΔR_{AHE} , as described by Eq. 4, evidently demonstrates an unconventional in-plane AHE with comparable magnitude to the conventional out-of-plane AHE. It is important to emphasize that the observed in-plane AHE cannot arise from a small out-of-plane magnetization component, given the soft magnetic properties of CGT and the fact that the measured total AHE resistance ΔR_{AHE} would immediately reverse sign across $\gamma_B = 90^\circ$ if it were solely associated with m_z .

Next, we focused on the in-plane AHE by fixing $\gamma_B = 90^\circ$ such that the magnetic field is aligned along the $\mathbf{y} \sim \mathbf{b}$ direction. We measured the temperature dependence of ΔR_{AHE}^y (Fig. 3f), where the in-plane AHE clearly vanishes near the Curie temperature (T_c) of CGT, further confirming that the observed unconventional in-plane AHE in TaIrTe₄ originates from the magnetism in the adjacent CGT layer.

Third, we investigated the gate voltage tunability of the unconventional in-plane AHE by measuring the R_{yx} versus B_y hysteresis loops at various gate voltages V_g (Fig. 3d). Interestingly, the extracted ΔR_{AHE}^y as a function of V_g , shown in Fig. 3e, exhibits a strong gate

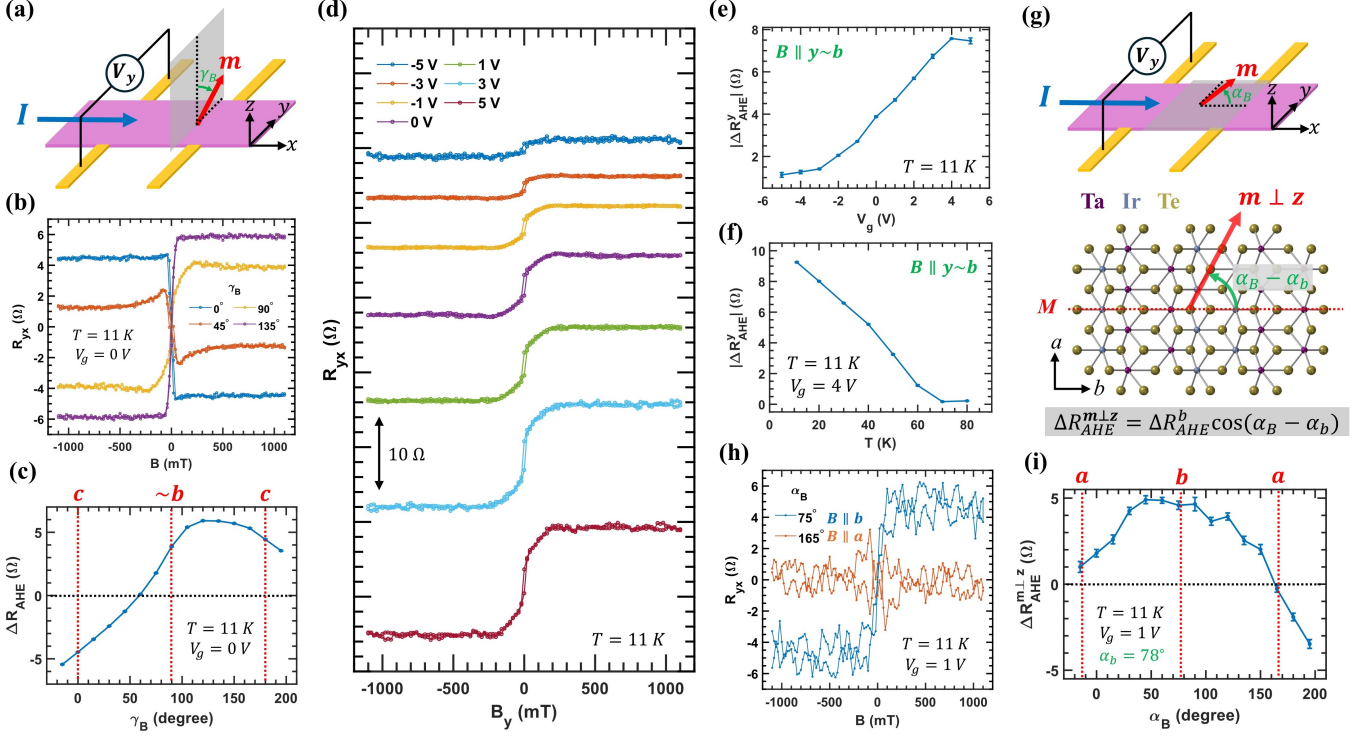


Fig. 3 In-plane magnetization induced AHE in TaIrTe₄/CGT system. **a**, Schematic showing the configuration for the Hall resistance measurements with the magnetization oriented at different zy -plane rotation angle (γ_B). **b**, The R_{yx} vs B hysteresis loops with the magnetic field at various zy -plane rotation angle γ_B . Note that the magnetic field is 12° away from b -axis of TaIrTe₄ when $B \parallel y$ ($\gamma_B = 90^\circ$). **c**, The measured AHE resistance, ΔR_{AHE} , as a function of γ_B . **d**, The R_{yx} vs B_y hysteresis loops at various V_g . **e**, The measured m_y -dependent AHE resistance, $\Delta R_{AHE}^{m_y}$, as a function of V_g . **f**, $\Delta R_{AHE}^{m_y}$ as a function of temperature. **g**, Upper panel: Schematic showing the configuration for the transverse resistance measurements with the magnetization oriented by the magnetic field at different xy -plane rotation angle (α_B). Lower panel: Illustration that the in-plane AHE, $\Delta R_{AHE}^{m \perp z}$, maximizes (vanishes) when the magnetization is aligned with the b -axis (a -axis) of TaIrTe₄. **h**, The R_{yx} vs B hysteresis loops with α_B at 75° ($B \parallel a$) and 165° ($B \parallel b$). The magnetic field is aligned with a -axis (b -axis) of TaIrTe₄ at $\alpha_B = 75^\circ$ ($\alpha_B = 165^\circ$). **i**, $\Delta R_{AHE}^{m \perp z}$ as a function of α_B .

voltage dependence, similar to that observed in ΔR_{AHE}^z . Within the accessible range of V_g , we observe a monotonic increase in ΔR_{AHE}^y with increasing gate voltage.

Finally, we investigated the dependence of the unconventional in-plane AHE on the magnetic orientation within the ab -plane of TaIrTe₄. To this end, we perform R_{yx} vs B hysteresis loop measurements with the in-plane magnetic field aligned at various in-plane rotation angles α_B relative to the current direction (x -axis), as illustrated in the upper panel of Fig. 3g. As shown in the lower panel of Fig. 3g, the symmetry of the TaIrTe₄/CGT heterostructure—where only the mirror symmetry with respect to the bc -plane is preserved—dictates that the in-plane component of the anomalous Hall effect follows the form:

$$\Delta R_{AHE}^{m \perp z}(\alpha_B) = \Delta R_{AHE}^b \cos(\alpha_B - \alpha_b), \quad (5)$$

indicating that the in-plane AHE response reaches its maximum (minimum) when the magnetic field is applied along the b -axis (a -axis) of TaIrTe₄.

In Fig. 3h, the hysteresis loops measured at different α_B , specifically at 75° ($B \parallel a$) and 165° ($B \parallel b$), show that the in-plane AHE is finite only when the magnetization has a component aligned with the b -axis of TaIrTe₄, and is zero when $m \parallel a$, consistent with the general form of AHE required by the symmetry of TaIrTe₄/CGT heterostructures. Note that the signal in the ab -plane rotation measurement is noisier because the device is

affected by cryogenic cooling cycles, necessary for mounting the device in the in-plane rotation position in our magnetotransport setup. The in-plane AHE resistance, $\Delta R_{AHE}^{m \perp z}$, as a function of α_B (Fig. 3i) is obtained by measuring the hysteresis loops in a range of α_B from -15° to 195° . In good agreement with our symmetry analysis and the crystal orientation of device A ($\alpha_b \sim 78^\circ$), the unconventional in-plane AHE term $\Delta R_{AHE}^{m \perp z}$ reaches a maximum when $m \parallel b$ and diminishes toward zero when $m \parallel a$.

Invariance of AHE under Rotations of current orientation

Next, we present experimental results from device B, shown in Fig. 4a (upper panel), which consists of a bilayer TaIrTe₄ and CGT. The pre-patterned Pt electrodes in device B are arranged in a 12-point disc geometry, with a 30° interval between adjacent electrodes. Device B is designed with two key objectives: first, to confirm that the observed unconventional in-plane AHE is not merely a consequence of the highly anisotropic electronic transport in TaIrTe₄; and second, to rigorously test the invariance of the AHE under rotations of the current orientation, thereby providing deeper insight into its underlying symmetry properties. The a -axis of TaIrTe₄ is only $\sim 5^\circ$ tilted from the vertical electrode in device B, verified by the polarized Raman spectroscopy (see Fig. S3). As shown in the lower panel of Fig. 4a, the longitudinal resistance is measured when the current is applied at different angles θ_I relative to the a -axis of TaIrTe₄. Due to the anisotropic

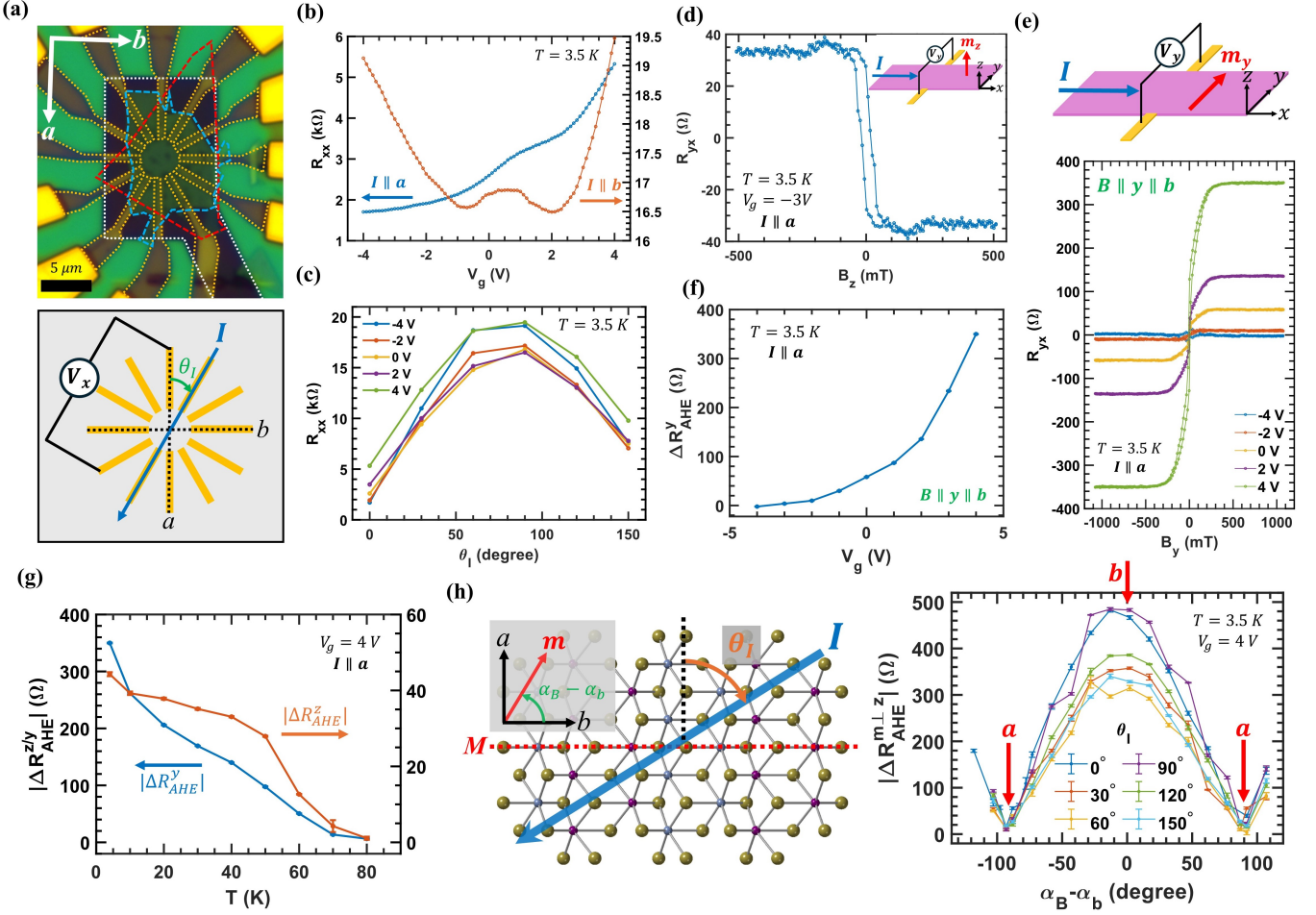


Fig. 4 Rotational invariance of in-plane AHE in TaIrTe₄/CGT system. **a**, Upper panel: Optical image of device B with the a -axis of TaIrTe₄ aligned close to one of the current electrodes ($\sim 5^\circ$ tilted), with CGT and TaIrTe₄ flakes outlined and labeled. The Pt electrodes (bottom gate) are outlined with dashed yellow (grey) lines. Lower panel: Schematic that charge current is applied at different angles θ_I relative to the a -axis of TaIrTe₄ while the longitudinal resistance is measured. **b**, The R_{xx} as a function of V_g when the charge current is applied along the a -axis ($\theta_I = 0^\circ$) and b -axis ($\theta_I = 90^\circ$) of TaIrTe₄. **c**, The R_{xx} as a function of θ_I at various V_g , where the resistance maximizes (minimizes) when the current is applied along the b - (a -) axis of TaIrTe₄. **d**, The R_{yx} vs B_z hysteresis loop with the non-AHE background signals removed. Inset: Schematic showing the configuration for the transverse resistance measurements with the magnetization oriented in the out-of-plane direction. **e**, Lower panel: The R_{yx} vs B_y hysteresis loops at various V_g . With the charge current applied along the a -axis of TaIrTe₄, the y -direction magnetic field is aligned with the b -axis of TaIrTe₄. Upper panel: Schematic showing the configuration for the transverse resistance measurements with the magnetization oriented in the y -direction. **f**, The measured m_y -dependent AHE resistance, ΔR_{AHE}^y , as a function of V_g . **g**, The m_y (m_z) dependent AHE resistance as a function of the temperature at $V_g = 4$ V when $I \parallel a$. **h**, Left panel: An illustration showing that the in-plane AHE magnitude, $|\Delta R_{AHE}^{m,\perp,z}|$, is measured when the in-plane magnetization is oriented, by applying an external magnetic field, at an angle of $\alpha_B - \alpha_b$ relative to the b -axis of TaIrTe₄, while the charge current is applied along various angle θ_I relative to the a -axis of TaIrTe₄. Right panel: The measured $|\Delta R_{AHE}^{m,\perp,z}|$ as a function of $\alpha_B - \alpha_b$ when the the charge current is applied at various θ_I .

transport in TaIrTe₄, the longitudinal resistance has a form of $R_{xx} = R_a \cos^2 \theta_I + R_b \sin^2 \theta_I$ [31, 32]. The R_{xx} as a function of V_g when $I \parallel a$ and $I \parallel b$ in Fig. 4b both show a peak near CNP ($V_g \simeq 1.5$ V), similar to device A. The increasing R_{xx} at high electron- and hole-doped regime might be due to the strong electron correlations induced by the formation of van Hove singularities, as previously reported in monolayer TaIrTe₄ devices [27]. To identify the anisotropic resistance, we plot R_{xx} as a function of θ_I at various gate voltages in Fig. 4c, showing that the longitudinal resistance reaches its maximum (minimum) when the current is applied along the b -axis (a -axis) of TaIrTe₄, consistent with our polarized Raman measurements.

Subsequently, we measured the R_{yx} vs B_z hysteresis loop and observed the conventional out-of-plane AHE, as shown in Fig. 4d. Next, we focus on the in-plane AHE signal in device B. We first measured the R_{yx} vs B_y

hysteresis loops in a range of V_g with $I \parallel a$ (and consequently $B \parallel b$), as shown in Fig. 4e. The extracted $\Delta R_{AHE}^y \simeq \Delta R_{AHE}^b$ as a function of V_g in device B, plotted in Fig. 4f, exhibits a V_g dependence similar to the ΔR_{AHE}^y observed in device A in Fig. 3e. The temperature dependence of both out-of-plane (in-plane) AHE resistance magnitude ($\Delta R_{AHE}^{z/y}$) measured at $V_g = 4$ V with $I \parallel a$ in Fig. 4g shows that AHE vanishes near the T_C of CGT, consistent with the results from device A. Finally, we examined the current direction dependence of the unconventional in-plane AHE by orienting the in-plane magnetization with an in-plane rotation angle of $\alpha_B - \alpha_b$ relative to the b -axis of TaIrTe₄ when the charge current is applied along different θ_I relative to the a -axis of TaIrTe₄, as illustrated by the schematic in the left panel of Fig. 4h. As verified by the $|\Delta R_{AHE}^{m,\perp,z}|$ as a function of $\alpha_B - \alpha_b$ with various θ_I in the right panel of Fig. 4, regardless of the applied current or voltage measurement

direction used to measure the transverse resistance, the results consistently show that in-plane AHE magnitude always reaches its maximum at $\alpha_B - \alpha_b = 0^\circ$ ($\mathbf{m} \parallel \mathbf{b}$) and vanishes at $\alpha_B - \alpha_b = \pm 90^\circ$ ($\mathbf{m} \parallel \mathbf{a}$). This observation is again in excellent agreement with the unique form of in-plane AHE in the TaIrTe₄/CGT system as required by the symmetry of C_s point group. In addition, our experimental findings further corroborate that the observed unconventional in-plane AHE is independent of the current orientation relative to the crystalline axes, as expected for an antisymmetric Hall effect.

Conclusion

Our work establishes a new paradigm for realizing unconventional forms of AHE in low-dimensional magnetic heterostructures. By interfacing a low-symmetry topological semimetal (TaIrTe₄) with a ferromagnetic insulator (CGT), we realized a low-dimensional material platform in which the Berry curvature distribution can be tuned by the reduced system symmetry, interface-induced SOC, and magnetic exchange couplings, allowing for the emergence of an unconventional AHE, i.e., an AHE signal proportional to both in-plane and out-of-plane magnetization. Through systematic experiments on multiple devices, we demonstrated that the AHE in TaIrTe₄/CGT presents when the CGT magnetization has a finite component along the remaining mirror (bc) plane of TaIrTe₄. Furthermore, we highlighted that the symmetry-controlled in-plane AHE reaches a maximum when the magnetization is aligned along the high-symmetry b -axis of TaIrTe₄, and vanishes when the magnetization is strictly along the a -axis, where the preserved mirror symmetry prohibits a Hall response, consistent with our theoretical symmetry analysis. Moreover, we observed a clear gate voltage dependence in both AHE components, indicating that the anomalous Hall effect in this 2D magnetic system is highly tunable via electrostatic control of the electron chemical potential. These findings provide a direct experimental manifestation of symmetry-engineered transport properties in low-symmetry quantum materials. Beyond confirming the role of symmetry in governing AHE, our results reveal the potential for designing tunable Hall effects by controlling crystal symmetry and exchange interactions at interfaces. Our work opens the possibilities of future investigations into other low-symmetry topological materials to engineer novel quantum transport for next-generation spintronic and electronic devices.

References

- [1] Xiao, D., Chang, M.-C. & Niu, Q. Berry phase effects on electronic properties. *Reviews of modern physics* **82**, 1959–2007 (2010).
- [2] Nagaosa, N., Sinova, J., Onoda, S., MacDonald, A. H. & Ong, N. P. Anomalous hall effect. *Reviews of modern physics* **82**, 1539–1592 (2010).
- [3] Karplus, R. & Luttinger, J. Hall effect in ferromagnetics. *Physical Review* **95**, 1154 (1954).
- [4] Luttinger, J. Theory of the hall effect in ferromagnetic substances. *Physical Review* **112**, 739 (1958).
- [5] Smit, J. The spontaneous hall effect in ferromagnetics ii. *Physica* **24**, 39–51 (1958).
- [6] Berger, L. Side-jump mechanism for the hall effect of ferromagnets. *Physical Review B* **2**, 4559 (1970).
- [7] Tan, H., Liu, Y. & Yan, B. Unconventional anomalous hall effect from magnetization parallel to the electric field. *Physical Review B* **103**, 214438 (2021).
- [8] Cao, J. *et al.* In-plane anomalous hall effect in pt-symmetric antiferromagnetic materials. *Physical Review Letters* **130**, 166702 (2023).
- [9] Zhang, Y. & Zhang, C. Quantized anomalous hall insulator in a nanopatterned two-dimensional electron gas. *Physical Review B—Condensed Matter and Materials Physics* **84**, 085123 (2011).
- [10] Wang, L. *et al.* Orbital magneto-nonlinear anomalous hall effect in kagome magnet fe 3 sn 2. *Physical Review Letters* **132**, 106601 (2024).
- [11] Liu, X., Hsu, H.-C. & Liu, C.-X. In-plane magnetization-induced quantum anomalous hall effect. *Physical review letters* **111**, 086802 (2013).
- [12] Liu, Z. *et al.* Intrinsic quantum anomalous hall effect with in-plane magnetization: searching rule and material prediction. *Physical Review Letters* **121**, 246401 (2018).
- [13] Sheoran, S. & Dev, P. Spontaneous anomalous hall effect in two-dimensional altermagnets. *arXiv preprint arXiv:2502.21095* (2025).
- [14] Li, D., Wang, M., Li, D. & Zhou, J. Switchable in-plane anomalous hall effect by magnetization orientation in monolayer mn 3 si 2 te 6. *Physical Review B* **109**, 155153 (2024).
- [15] Kumar, N., Soh, Y., Wang, Y., Li, J. & Xiong, Y. Anomalous planar hall effect in a kagome ferromagnet. *arXiv preprint arXiv:2005.14237* (2020).
- [16] Wang, L. *et al.* In-plane hall effect in co₃sn₂s₂. *Phys. Rev. B* **111**, 054412 (2025).
- [17] Nakamura, A. *et al.* In-plane anomalous hall effect associated with orbital magnetization: Measurements of low-carrier density films of a magnetic weyl semimetal. *Physical Review Letters* **133**, 236602 (2024).
- [18] Liang, T. *et al.* Anomalous hall effect in zrte₅. *Nature Physics* **14**, 451–455 (2018).
- [19] Galeski, S. *et al.* Unconventional hall response in the quantum limit of hfte₅. *Nature communications* **11**, 5926 (2020).

- [20] Ge, J. *et al.* Unconventional hall effect induced by berry curvature. *National science review* **7**, 1879–1885 (2020).
- [21] Peng, W. *et al.* Observation of the in-plane anomalous hall effect induced by octupole in magnetization space. *arXiv preprint arXiv:2402.15741* (2024).
- [22] Zhou, J. *et al.* Heterodimensional superlattice with in-plane anomalous hall effect. *Nature* **609**, 46–51 (2022).
- [23] Liu, Y. & Shao, Q. Two-dimensional materials for energy-efficient spin–orbit torque devices. *ACS nano* **14**, 9389–9407 (2020).
- [24] Koepernik, K. *et al.* Tairte 4: A ternary type-ii weyl semimetal. *Physical Review B* **93**, 201101 (2016).
- [25] Haubold, E. *et al.* Experimental realization of type-ii weyl state in noncentrosymmetric tairte 4. *Physical Review B* **95**, 241108 (2017).
- [26] Guo, P.-J., Lu, X.-Q., Ji, W., Liu, K. & Lu, Z.-Y. Quantum spin hall effect in monolayer and bilayer tairte 4. *Physical Review B* **102**, 041109 (2020).
- [27] Tang, J. *et al.* Dual quantum spin hall insulator by density-tuned correlations in tairte4. *Nature* **628**, 515–521 (2024).
- [28] Zhang, X. *et al.* Magnetic anisotropy of the single-crystalline ferromagnetic insulator cr2ge2te6. *Japanese Journal of Applied Physics* **55**, 033001 (2016).
- [29] Gong, C. *et al.* Discovery of intrinsic ferromagnetism in two-dimensional van der waals crystals. *Nature* **546**, 265–269 (2017).
- [30] Onsager, L. Reciprocal relations in irreversible processes. ii. *Physical review* **38**, 2265 (1931).
- [31] Liu, Y. *et al.* Raman signatures of broken inversion symmetry and in-plane anisotropy in type-ii weyl semimetal candidate tairte4. *Advanced Materials* **30**, 1706402 (2018).
- [32] Li, D. *et al.* Room-temperature van der waals magnetoresistive memories with data writing by orbital current in the weyl semimetal tairt e 4. *Physical Review B* **110**, 035423 (2024).
- [33] Kao, I.-H. *et al.* Deterministic switching of a perpendicularly polarized magnet using unconventional spin–orbit torques in wte2. *Nature materials* **21**, 1029–1034 (2022).
- [34] Kao, I.-H. *et al.* Unconventional unidirectional magnetoresistance in heterostructures of a topological semimetal and a ferromagnet. *Nature Materials* 1–9 (2025).
- [35] Liu, Y. *et al.* Field-free switching of perpendicular magnetization at room temperature using out-of-plane spins from tairte4. *Nature Electronics* **6**, 732–738 (2023).
- [36] Zhuo, W. *et al.* Manipulating ferromagnetism in few-layered cr2ge2te6. *Advanced Materials* **33**, 2008586 (2021).
- [37] Wang, Z. *et al.* Electric-field control of magnetism in a few-layered van der waals ferromagnetic semiconductor. *Nature nanotechnology* **13**, 554–559 (2018).
- [38] Carteaux, V., Brunet, D., Ouvrard, G. & Andre, G. Crystallographic, magnetic and electronic structures of a new layered ferromagnetic compound cr2ge2te6. *Journal of Physics: Condensed Matter* **7**, 69 (1995).
- [39] Lohmann, M. *et al.* Probing magnetism in insulating cr2ge2te6 by induced anomalous hall effect in pt. *Nano letters* **19**, 2397–2403 (2019).
- [40] Lu, Y. *et al.* Hybrid magnetoresistance in the proximity of a ferromagnet. *Physical Review B—Condensed Matter and Materials Physics* **87**, 220409 (2013).
- [41] Mogi, M. *et al.* Large anomalous hall effect in topological insulators with proximitized ferromagnetic insulators. *Physical review letters* **123**, 016804 (2019).
- [42] Llacsahuanga Allica, A. E., Pan, X.-C., Miotkowski, I., Tanigaki, K. & Chen, Y. P. Gate-tunable anomalous hall effect in stacked van der waals ferromagnetic insulator–topological insulator heterostructures. *Nano Letters* **22**, 8130–8136 (2022).
- [43] Chong, S. K. *et al.* Topological insulator-based van der waals heterostructures for effective control of massless and massive dirac fermions. *Nano Letters* **18**, 8047–8053 (2018).
- [44] Gupta, V. *et al.* Gate-tunable anomalous hall effect in a 3d topological insulator/2d magnet van der waals heterostructure. *Nano Letters* **22**, 7166–7172 (2022).
- [45] Jain, R. *et al.* A quantized anomalous hall effect above 4.2 k in stacked topological insulator/magnet bilayers. *arXiv preprint arXiv:2412.05380* (2024).
- [46] Cai, S. *et al.* Observation of superconductivity in the pressurized weyl-semimetal candidate tairt e 4. *Physical Review B* **99**, 020503 (2019).
- [47] Liu, S. *et al.* Single crystal growth of millimeter-sized monoisotopic hexagonal boron nitride. *Chemistry of materials* **30**, 6222–6225 (2018).

Methods

Device Fabrication

TaIrTe₄ and hexagonal boron nitride (h-BN) crystals were prepared using previously published procedures [46, 47]. Cr₂Ge₂Te₆ (CGT) single crystals were purchased from HQ Graphene. Mechanical exfoliation of TaIrTe₄,

Cr₂Ge₂Te₆ (CGT), h-BN, and graphite was performed on separate silicon wafers with 300 nm of SiO₂ inside a glovebox filled with Ar gas. Flakes were selected through optical investigation through a microscope. TaIrTe₄ flakes that have well-defined and straight edges were used because the *a*-axis tends to be along them.

The heterostructure was fabricated using a custom transfer tool inside a glovebox filled with Ar gas. A transfer slide consisting of a polydimethylsiloxane (PDMS) slab and a thin film of polycarbonate (PC) was used for transfer 2D flakes. The electrodes for electric connection are patterned using electron beam lithography (EBL) and electron beam deposition with a PMMA/MMA bilayer resist. The bottom h-BN is transferred on top of a bottom Pt or graphite gate prepared on the Si/SiO₂ substrate, and Pt electrodes composed of Ti (2 nm)/Pt (6 nm) were patterned on top of the h-BN. The Pt electrodes were then connected by Cr (5 nm)/Au (55 nm) electrodes for wire bonding pads. The Pt electrodes and bottom h-BN were cleaned by atomic force microscopy in contact mode using μ masch HQ:NSC15/Al BS tips and ultra-high vacuum annealing at 200°C for 4 hours before the heterostructure of TaIrTe₄/CGT/h-BN was transferred to the electrodes to ensure the interface quality. For devices with a top gate (Device D), an additional graphite flake is picked up in the beginning to contact the pre-patterned Pt electrodes.

Device Characterization

To determine the thickness and the crystallographic orientation of the TaIrTe₄/CGT devices, we utilize AFM and polarized Raman spectroscopy. All the devices were examined by AFM in the tapping mode using μ masch HQ: NSC15/ Al BS tip to investigate the thickness of flakes used in each device. The TaIrTe₄ thickness is characterized by a combination of optical contrast and AFM. The crystallographic orientation of TaIrTe₄ in device A, B, and D were confirmed by angle-dependent Polarized Raman measurements. We focused on the Raman shift peak of TaIrTe₄ A₁ mode at around 148.5 cm⁻¹ to determine the crystallographic orientations of the TaIrTe₄ flake [27, 31, 35]. The Raman intensity of A₁ mode is maximized when laser polarization is parallel to the *a*-axis of TaIrTe₄.

Electrical measurements

Electrical measurements were performed at variable temperatures under high vacuum (< 10⁻⁵ mtorr) conditions. An electromagnet was rotated such that the magnetic field could be rotated in *xy* or *zy* plane depending on the mounting orientation of the device. For device A and B, a Keithley 6221 current source is used to apply a sinusoidal AC current of 1 μ A at 111.37 Hz, while an SR830 Lock-In Amplifier (Signal Recovery 7265 DSP Lock-in Amplifier) is used to measure the first harmonic transverse (longitudinal) voltage. For device C and D, a Keithley 6221 current source is used to apply a positive and negative DC current in the range of 1 – 10 μ A, while two Keithley 2182A nanovoltmeters are used for DC measurements for transverse and longitudinal resistances. The results obtained by DC methods are symmetrized with respect to the current polarity. Keithley 2400 and 2450 source meters are used for applying gate voltage to the device.

The Hall effects are antisymmetric to the B-field, therefore the measured transverse resistance is first anti-symmetrized with respect to B-field to better quantify the observed unconventional AHE. This is achieved by measuring the full magnetic hysteresis loop ($-B \rightarrow +B$ and $+B \rightarrow -B$), calculating the transverse Hall resistance by $R_{yx}(B) = \frac{1}{2}[R_{yx,raw}(B) - R_{yx,raw}(-B)]$ between the forward and backward loops. Some raw transverse resistance R_{yx} vs B-field results used in the main text are shown in Fig.S1.

Minimal microscopic two-band model

We propose an intrinsic origin of the observed AHE, namely, a Hall conductivity induced by Berry curvature of the system. To this end, we write down a minimal effective Hamiltonian that is constrained by the relevant symmetries, and analyze the resultant Hall conductivity. Since the symmetries of few-layered TaIrTe₄ are described by the C_{2v} point group, which is composed of $\{e, C_2, M_a, M_b\}$, plus the time-reversal operator \mathcal{T} , we list the actions of the group elements on momentum and spin below:

$$\begin{aligned} C_2 : (k_a, k_b) &\rightarrow (-k_a, -k_b), (s^a, s^b, s^c) \rightarrow (-s^a, -s^b, s^c) \\ M_a : (k_a, k_b) &\rightarrow (-k_a, k_b), (s^a, s^b, s^c) \rightarrow (s^a, -s^b, -s^c) \\ M_b : (k_a, k_b) &\rightarrow (k_a, -k_b), (s^a, s^b, s^c) \rightarrow (-s^a, s^b, -s^c) \\ \mathcal{T} : (k_a, k_b) &\rightarrow (-k_a, -k_b), (s^a, s^b, s^c) \rightarrow (-s^a, -s^b, -s^c) \end{aligned}$$

Note that $M_a M_b = C_2$, so we only need to consider one of the mirrors, say M_a .

Given these symmetries, the most general two-band Hamiltonian that can be written in an expansion in momentum (upto second order) is

$$H_0 = \frac{k_a^2}{2\tilde{m}_a} + \frac{k_b^2}{2\tilde{m}_b} + g_{ab}k_a s^b + g_{ba}k_b s^a$$

If $g_{ab} = -g_{ba}$, then the spin-orbit coupling (SOC) term takes the form $(\mathbf{k} \times \mathbf{s}) \cdot \hat{\mathbf{z}}$, which is the conventional Rashba SOC. This constraint is typically enforced by a larger rotational symmetry about the *c*-axis, but g_{ab} and g_{ba} can be independent if only C_2 is present. The Berry curvature changes sign under the action of $C_2 \mathcal{T}$, which is a preserved symmetry of TaIrTe₄, so the Berry curvature must be zero and therefore any intrinsic contribution to AHE is forbidden. One can simply add magnetization in the *c*-direction to break $C_2 \mathcal{T}$ and the mirror symmetry and get a non-zero anomalous Hall conductivity. However, an in-plane magnetization by itself is odd under both C_2 and \mathcal{T} , and consequently does not break $C_2 \mathcal{T}$. Therefore no in-plane AHE is allowed when we have $C_2 \mathcal{T}$, and the symmetry of the system needs to be lowered.

To achieve the desired lower symmetry, a material with point group C_{2v} , such as TaIrTe₄, is interfaced with a magnetic material like CGT to break C_2 . In this case, the point group is reduced to $C_s = \{e, M_a\}$ even in the absence of magnetization \mathbf{m} in the magnetic material. Now, additional combinations of momentum and spin, namely, $k_a s^c$ and $k_b s^c$ are symmetry-allowed in the Hamiltonian (the inclusion of the cubic term is required to avoid a fine-tuned limit, as we will explain later). Furthermore, we

include the exchange interactions from the magnetization, so the Hamiltonian becomes

$$H = H_0 + g_{ac}k_a s^c + \tilde{g}_{ac}k_a^3 s^c - \Delta_{ex}\mathbf{m} \cdot \mathbf{s}$$

where the time-reversal symmetry can be broken by the magnetization to allow for AHE. Next, we compute the anomalous Hall conductance when \mathbf{m} points along each of the crystalline axes. For simplicity, we will set the effective masses $\tilde{m}_a = \tilde{m}_b = \tilde{m}$ for the rest of the discussion.

When \mathbf{m} is in the b -direction, the mirror symmetry \mathcal{M}_a is broken. In this case, the dispersions of the two bands are given by

$$\varepsilon_{1,2}(\mathbf{k}) = \frac{k^2}{2\tilde{m}} \pm \sqrt{(E_{ab} - m)^2 + E_{ba}^2 + E_{ac}^2}$$

and the Berry curvatures of the two bands [1] are

$$\Omega_{1,2}(\mathbf{k}) = \pm \frac{m(g_{ba}g_{ac} + 3g_{ba}\tilde{g}_{ac}k_a^2) - 2g_{ab}g_{ba}\tilde{g}_{ac}k_a^3}{2[(E_{ab} - m)^2 + E_{ba}^2 + E_{ac}^2]^{\frac{3}{2}}}$$

where $E_{ab} = g_{ab}k_a$, $E_{ba} = g_{ba}k_b$, and $E_{ac} = g_{ac}k_a + \tilde{g}_{ac}k_a^3$. Note that the Berry curvature is neither even nor odd under $k_a \rightarrow -k_a$, and this asymmetry is responsible for a non-zero anomalous Hall conductance. Specifically, the anomalous Hall conductivity [?] is then given by

$$\sigma_{ab} = \sum_{n=1,2} -\frac{e^2}{\hbar} \iint n_F(\varepsilon_n(\mathbf{k})) \Omega_n(\mathbf{k}) \frac{dk_a dk_b}{(2\pi)^2}$$

where n_F is the Fermi-Dirac distribution. In the $T \rightarrow 0$ limit, the integral runs over all the occupied states, chosen to be $[-0.01, 0.01]nm^{-1}$ in both directions to cover all the space where the Berry curvature is significant. The resultant Hall conductance for $\mathbf{m} \parallel \mathbf{b}$ is shown in Fig. S8(g).

We can apply this approach to calculate the anomalous Hall response for the magnetization vector pointing in other directions too. In particular, let us explicitly see why the anomalous Hall conductance must be zero when the magnetization \mathbf{m} is along the a -axis and the system preserves \mathcal{M}_a symmetry. In this limit, the band dispersions are

$$\varepsilon_{1,2}(\mathbf{k}) = \frac{k^2}{2\tilde{m}} \pm \sqrt{E_{ab}^2 + (E_{ba} - m)^2 + E_{ac}^2}$$

while the Berry curvatures take the form

$$\Omega_{1,2}(\mathbf{k}) = \pm \frac{g_{ab}g_{ba}\tilde{g}_{ac}k_a^3}{[E_{ab}^2 + (E_{ba} - m)^2 + E_{ac}^2]^{\frac{3}{2}}}$$

We note that the Berry curvatures $\Omega_{1,2}(\mathbf{k})$ would vanish if we did not include the cubic term $\tilde{g}_{ac}k_a^3 s^c$, making this example too fine-tuned.

From our computations, we can explicitly see that the dispersions are even under $k_a \rightarrow -k_a$, i.e., $\varepsilon_{1,2}(k_a, k_b) = \varepsilon_{1,2}(-k_a, k_b)$, while the Berry curvature is odd under $k_a \rightarrow -k_a$, i.e., $\Omega_{1,2}(k_a, k_b) = -\Omega_{1,2}(-k_a, k_b)$, as expected for a pseudoscalar in 2D. This is a consequence of preserving the mirror symmetry \mathcal{M}_a , and the resultant Hall

conductance can be shown to vanish by acting \mathcal{M}_a on the integrand, as follows:

$$\begin{aligned} \sigma_{ab} &= -\frac{e^2}{\hbar} \sum_{n=1,2} \iint n_F[\varepsilon_n(-k_a, k_b)] \Omega_n(-k_a, k_b) \frac{dk_a dk_b}{(2\pi)^2} \\ &= -\frac{e^2}{\hbar} \sum_{n=1,2} \iint n_F[\varepsilon_n(k_a, k_b)] (-\Omega_n(k_a, k_b)) \frac{dk_a dk_b}{(2\pi)^2} \\ &= -\sigma_{ab} \implies \sigma_{ab} = 0 \end{aligned}$$

For completeness, we also write down the expressions of band dispersions and Berry curvatures for magnetization \mathbf{m} along the c -axis:

$$\varepsilon_{1,2}(\mathbf{k}) = \frac{k^2}{2\tilde{m}} \pm \sqrt{E_{ab}^2 + E_{ba}^2 + (E_{ac} - m)^2},$$

and

$$\Omega_{1,2}(\mathbf{k}) = \mp \frac{g_{ab}g_{ba}(m + 2\tilde{g}_{ac}k_a^3)}{2[E_{ab}^2 + E_{ba}^2 + (E_{ac} - m)^2]^{\frac{3}{2}}}.$$

We summarize our results in Fig. S8. With reasonable parameters, the model yields a finite and physically consistent anomalous Hall conductivity. Theoretical results are shown for both in-plane and out-of-plane magnetization configurations, offering a qualitative explanation for the emergence of unconventional AHE in magnetic systems with \mathcal{C}_s symmetry, such as TaIrTe₄/CGT heterostructures. The key ingredients in our model are the spin-orbit coupling (SOC) terms $k_a s^c$ and $k_a^3 s^c$ that are symmetry-allowed (even though we do not comment on their microscopic origin), along with the exchange coupling $\Delta_{ex}\mathbf{m} \cdot \mathbf{s}$. If the observed AHE is primarily driven by Berry curvature, these terms offer a natural and minimal explanation. We emphasize that this model is not intended to quantitatively match experimental data, but rather to propose a simple, symmetry-based, microscopic picture that captures the essential physics of our experimental observations.

Acknowledgments

S.S. acknowledges the financial support from U.S. Office of Naval Research under Award No. N00014-23-1-2751, National Science Foundation (NSF) through Grants No. ECCS-2208057 and DMR-2210510, and from the Center for Emergent Materials at The Ohio State University, a National Science Foundation (NSF) MRSEC, through Award No. DMR-2011876. S.S. also acknowledges financial support from NSF-CAREER Award through Grant No. ECCS-2339723. J.K. acknowledges the financial support from U.S. Office of Naval Research under Award No. N00014-23-1-2751, the Center for Emergent Materials at The Ohio State University, an NSF MRSEC, through Award No. DMR-2011876, and the U.S. Department Office of Science, Office of Basic Sciences, of the U.S. Department of Energy through award No. DE-SC0020323 (for device fabrication). J.K. also acknowledges financial support from NSF-CAREER Award under Grant No. DMR-2339309. The single crystal growth and characterization of TaIrTe₄ at UCLA were supported by the U.S. Department of Energy (DOE), Office of

Science, Office of Basic Energy Sciences under Award Number DE-SC0021117. J.H.E. acknowledges the support for hBN crystal growth from the U. S. Office of Naval Research under award number N00014-22-1-2582. K.W. and T.T. acknowledge support from the JSPS KAKENHI (Grant Numbers 21H05233 and 23H02052), the CREST (JPMJCR24A5), JST and World Premier International Research Center Initiative (WPI), MEXT, Japan. We acknowledge Archibald J. Williams for providing the schematic of TaIrTe₄ crystal structure used in the manuscript Figures. The authors also thank Ran Cheng and Junyu Tang for insightful discussions.

Author Contributions

S.S. and J.K. supervised the research. I.K. and R.K.B. prepared the devices, performed measurements, and analyzed the data with assistance of Z.C., S.S., A.T., and M.C. J.T., Q.M., and S.Y.X provided the support for sample and device preparation. S.Z. and S.C. provided the theoretical support. R.R. carried out polarized Raman measurements. T.Q. and N.N. grew the bulk crystals of TaIrTe₄. J.L., J. H. E., K.W., and T.T. provided the bulk h-BN crystals. All authors contributed to write the manuscript.

Competing interests

The authors declare no competing interests.

Supplementary Information

Table S1 The TaIrTe₄ alignment, electrode geometry, and thickness parameters of TaIrTe₄, CGT, thBN, and bhBN flakes in TaIrTe₄/CGT devices.

Device	t_{TaIrTe_4} (nm)	t_{CGT} (nm)	t_{thBN} (nm)	t_{bhBN} (nm)	Electrode geometry
A	1.6 (Bilayer)	11.9	12.4	6.6	Hall bar
B	1.4 (Bilayer)	8.3	20.2	5.3	12-point disc
C	2.4 (Trilayer)	11.2	18.9	41.1	Hall bar
D	Bilayer	8.0	20.2	5.3	Hall bar

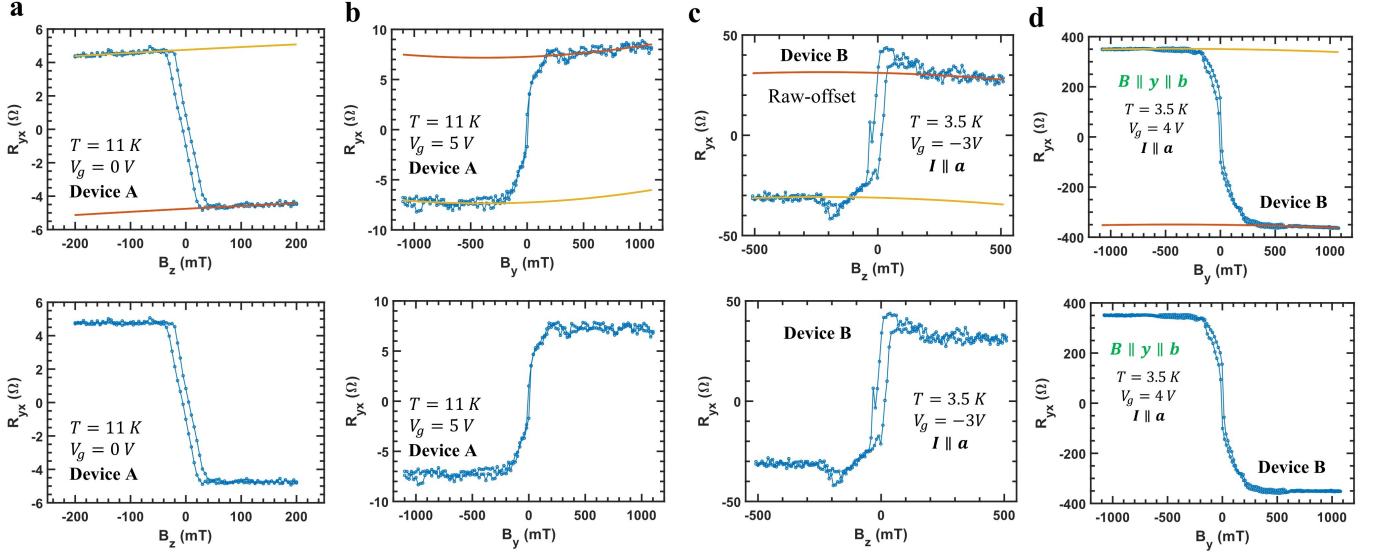


Fig. S1 Transverse resistance hysteresis loops before magnetic field symmetrization. **a**, Raw transverse resistance (R_{yx}) vs B_z in Fig. 2e before anti-symmetrization relative to the magnetic field with the offset removed (upper panel) and after the removal of non-AHE background up to 2nd order polynomials (lower panel). **b**, Raw transverse resistance (R_{yx}) vs B_y at $V_g = 5$ V in Fig. 3d before anti-symmetrization relative to the magnetic field with the offset removed (upper panel) and after the removal of non-AHE background up to 2nd order polynomials (lower panel). **c**, Raw transverse resistance (R_{yx}) vs B_z in Fig. 4d before anti-symmetrization relative to the magnetic field with the offset removed (upper panel) and after the removal of non-AHE background up to 2nd order polynomials (lower panel). **d**, Raw transverse resistance (R_{yx}) vs B_y at $V_g = 5$ V in Fig. 4e before anti-symmetrization relative to the magnetic field with the offset removed (upper panel) and after the removal of non-AHE background up to 2nd order polynomials (lower panel).

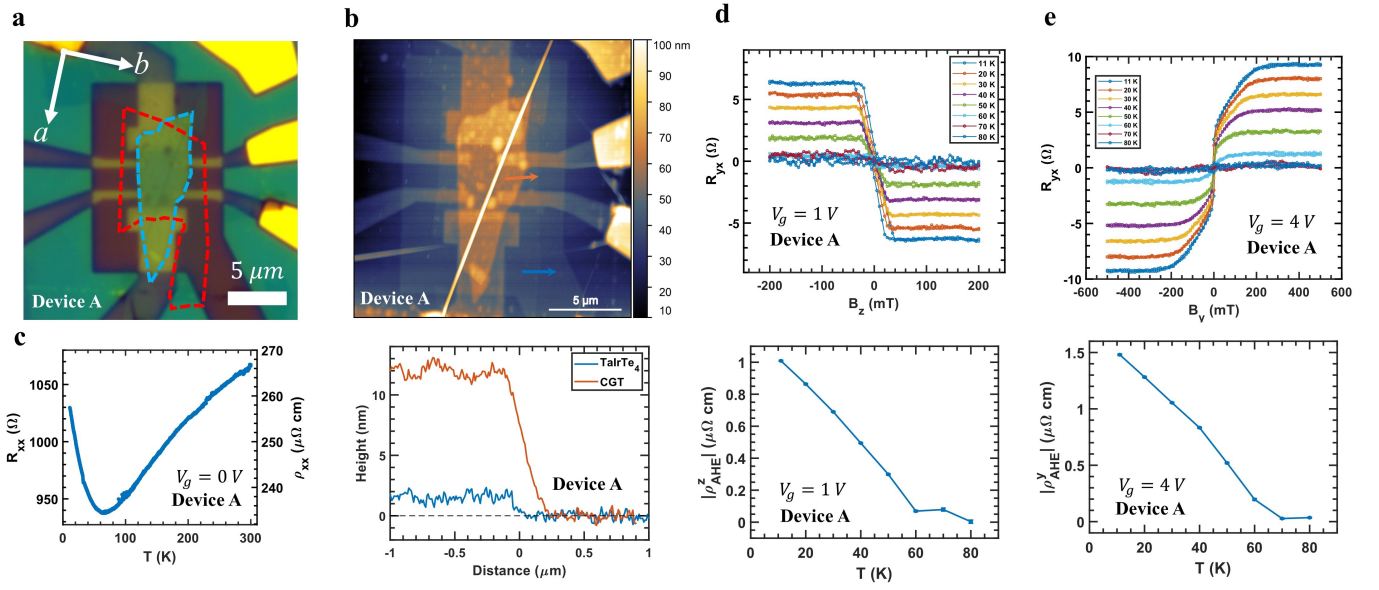


Fig. S2 Device A: Characterization, transport property, and additional temperature dependence results **a**, Optical micrograph of device A, where the TaIrTe₄ (dashed red) and CGT (dashed cyan) flakes are outlined. In device A, the angle between the *b*-axis and the current channel is $\alpha_b = 78^\circ$. **b**, AFM topography map of device A (upper panel) and the height line scans of TaIrTe₄ and CGT (lower panel) taken around arrow indications in the map. **c**, The longitudinal resistance (resistivity) of device A as a function of temperature. **d**, Upper panel: The R_{yx} vs B_z hysteresis loops measured in device A at various temperatures. Lower panel: The m_z -dependent AHE resistivity magnitude ($|\rho_{z_{AHE}}|$) in device A as a function of temperature. **e**, Upper panel: The R_{yx} vs B_y hysteresis loops measured in device A at various temperatures. Lower panel: The m_y -dependent AHE resistivity magnitude ($|\rho_{y_{AHE}}|$) in device A as a function of temperature. Note that in the orientation of device A, $|\rho_{y_{AHE}}| = \sin \alpha_b |\rho_{z_{AHE}}| \simeq |\rho_{z_{AHE}}|$.

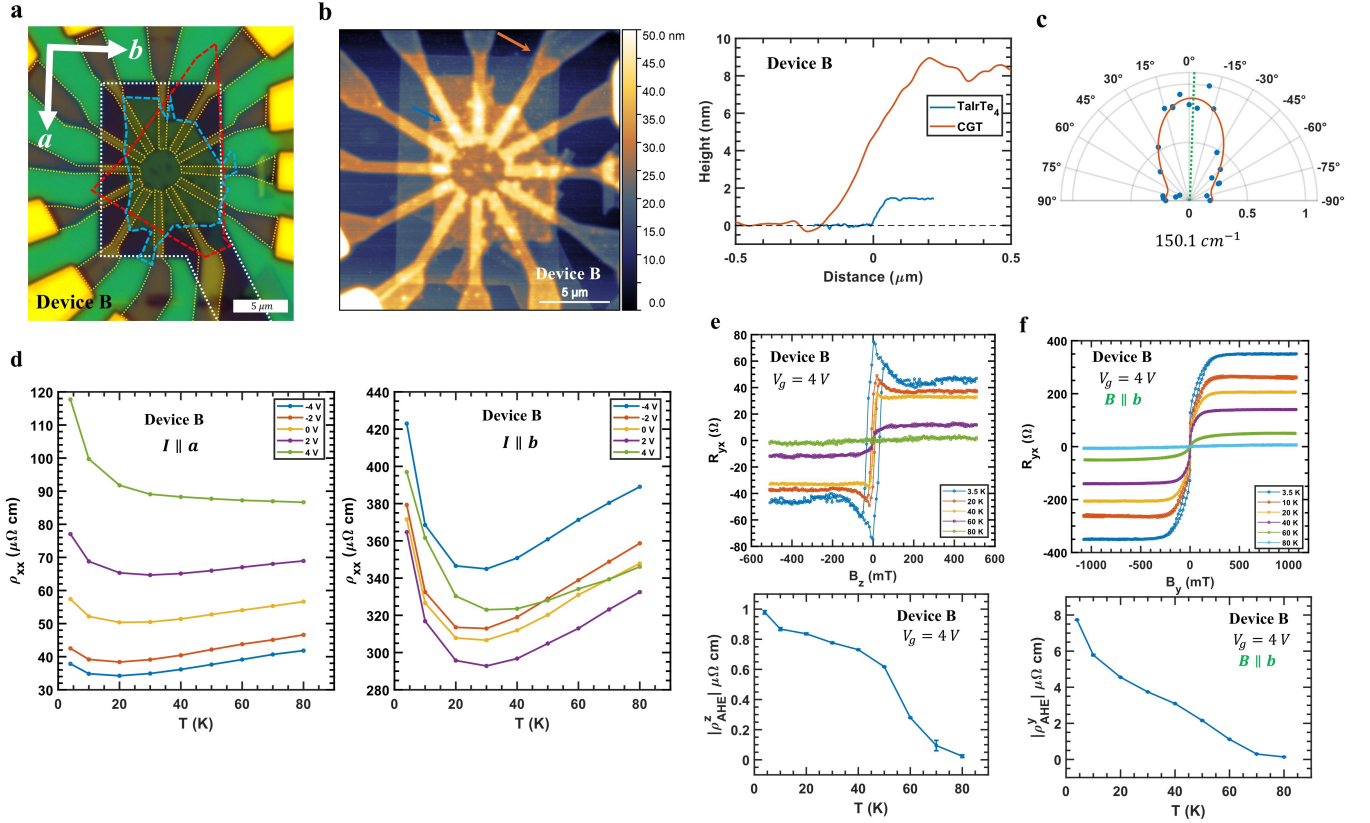


Fig. S3 Device B: Characterization, transport property, and additional temperature dependence results **a**, Optical micrograph of device B, where the TaIrTe₄ (dashed red), CGT (dashed cyan) flakes, Pt electrodes (dashed yellow), and bottom Pt gate (dashed gray) are outlined. In device B, the angle between the *b*-axis and the current channel is $\alpha_b = 95^\circ$. **b**, AFM topography map of device B (left panel) and the height line scans of TaIrTe₄ and CGT (right panel) taken around arrow indications in the map. **c**, The Angle-dependent polarized Raman spectral intensity at 150.1 cm^{-1} of TaIrTe₄ flake relative to the vertical current channel in device B. **d**, The longitudinal resistivity of device B as a function of temperature at various gate voltages when the charge current is applied along the *a*-axis (left panel) and the *b*-axis (right panel) of TaIrTe₄. **e**, Upper panel: The R_{yx} vs B_z hysteresis loops measured in device B at various temperatures. Lower panel: The m_z -dependent AHE resistivity magnitude ($|\rho_{AHE}^z|$) in device B as a function of temperature. **f**, Upper panel: The R_{yx} vs B_y hysteresis loops measured in device B at various temperatures when $I \parallel a$ ($B \parallel b$). Lower panel: The m_y -dependent AHE resistivity magnitude ($|\rho_{AHE}^y|$) in device B as a function of temperature. Note that in the orientation of device B when $I \parallel a$, $|\rho_{AHE}^y| = \sin \alpha_b |\rho_{AHE}^b| \simeq |\rho_{AHE}^b|$.

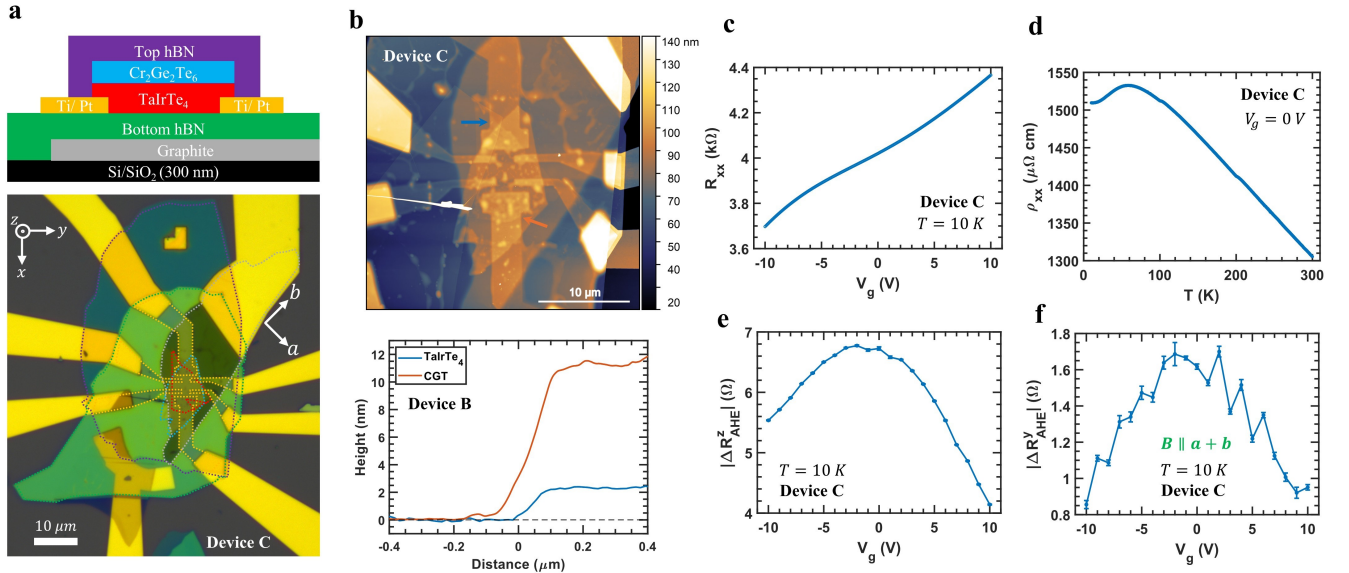


Fig. S4 Device C: Characterization, transport property, and gate voltage dependence results **a**, The schematic of the device C side view (upper panel) and the optical micrograph of device C (lower panel), where the TaIrTe₄ (dashed red), CGT (dashed cyan), bottom h-BN (dashed green), top h-BN (dashed purple) flakes, Pt electrodes (dashed yellow), and bottom graphite gate (dashed gray) are outlined. In device C, the angle between the *b*-axis and the current channel is $\alpha_b = 45^\circ$. **b**, AFM topography map of device C (upper panel) and the height line scans of TaIrTe₄ and CGT (lower panel) taken around arrow indications in the map. **c**, The longitudinal resistance of device C as a function of gate voltage at 10 K. **d**, The longitudinal resistivity of device C as a function of temperature. **e**, The m_z -dependent AHE resistance magnitude ($|\Delta R_{AHE}^z|$) in device C as a function of gate voltage. **f**, The m_y -dependent AHE resistance magnitude ($|\Delta R_{AHE}^y|$) in device C as a function of gate voltage. Note that in the orientation of device C, $|\Delta R_{AHE}^y| = \sin \alpha_b |\Delta R_{AHE}^b| \simeq 0.71 |\Delta R_{AHE}^b|$.

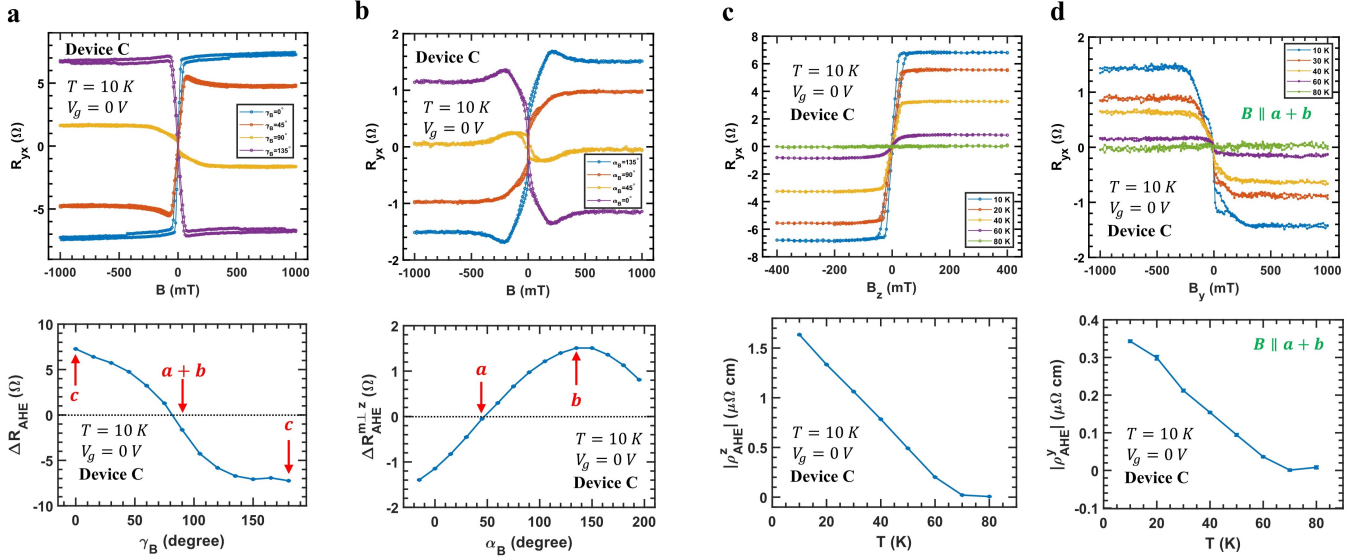


Fig. S5 Device C: Magnetic field angle and temperature dependence results **a**, Upper panel: The R_{yx} vs B hysteresis loops measured in device C at various zy -plane rotation angle γ_B . Lower panel: The total AHE resistance (ΔR_{AHE}) in device C as a function of γ_B . Note that in the orientation of device C, when $\gamma_B = 90^\circ$, $B \parallel a+b$. **b**, Upper panel: The R_{yx} vs B hysteresis loops measured in device C at various xy -plane rotation angle α_B relative to the current direction (x -axis) Lower panel: The in-plane AHE resistance ($\Delta R_{AHE}^{m\perp z}$) in device C as a function of α_B . **c**, Upper panel: The R_{yx} vs B_z hysteresis loops measured in device C at various temperatures. Lower panel: The m_z -dependent AHE resistivity magnitude ($|\rho_{AHE}^z|$) in device C as a function of temperature. **d**, Upper panel: The R_{yx} vs B_y hysteresis loops measured in device C at various temperatures. Lower panel: The m_y -dependent AHE resistivity magnitude ($|\rho_{AHE}^y|$) in device C as a function of temperature. Note that in the orientation of device C, $|\rho_{AHE}^y| = \sin \alpha_b |\rho_{AHE}^b| \simeq 0.71 |\rho_{AHE}^b|$.

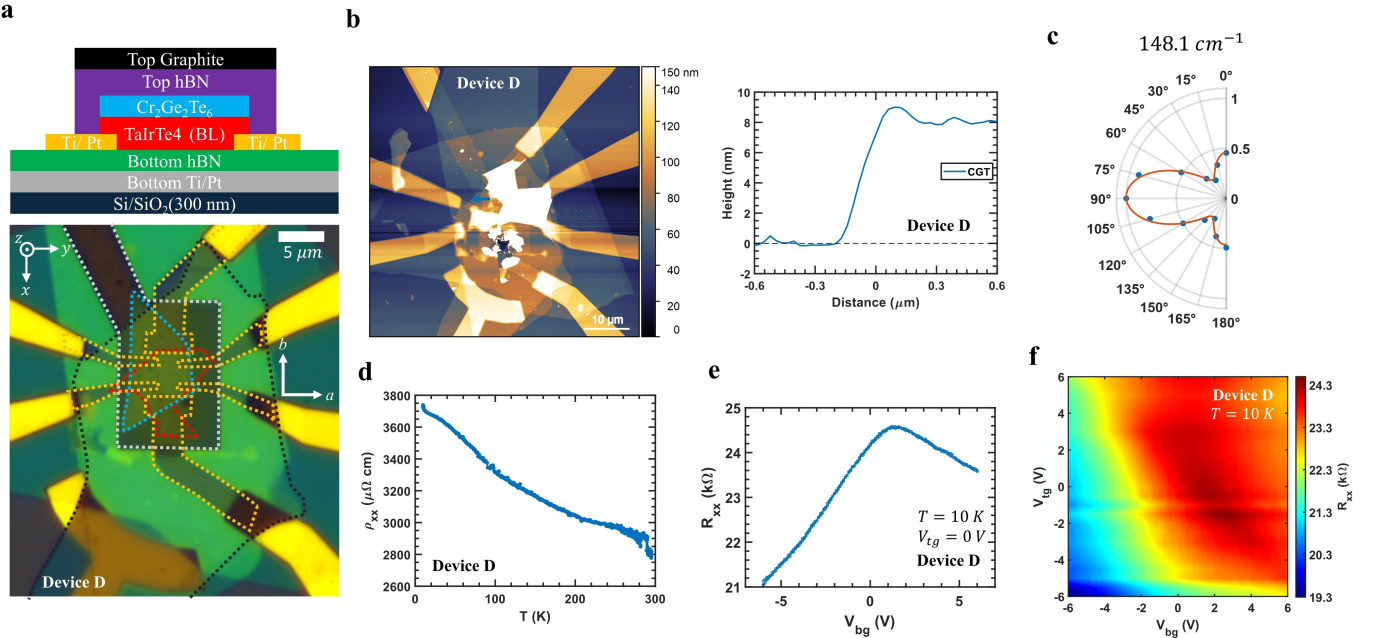


Fig. S6 Device D: Characterization and transport property **a**, The schematic of the device D side view (upper panel) and the optical micrograph of device D (lower panel), where the TaIrTe₄ (dashed red), CGT (dashed cyan) flakes, Pt electrodes (dashed yellow), bottom Pt gate (dashed gray), and top graphite gate (dashed black) are outlined. In device D, the angle between the b -axis and the current channel is $\alpha_b \simeq 0^\circ$. **b**, AFM topography map of device D (left panel) and the height line scans of CGT flake (right panel) taken around arrow indications in the map. The device D is damaged after the measurements thus no AFM thickness characterization on TaIrTe₄ is performed. **c**, The Angle-dependent polarized Raman spectral intensity at 148.1 cm^{-1} of TaIrTe₄ flake relative to the vertical current channel in device D. **d**, The longitudinal resistivity of device D as a function of temperature. **e**, The longitudinal resistance of device D as a function of the bottom gate voltage (V_{bg}) at $T = 10\text{ K}$ when $V_{tg} = 0\text{ V}$. **f**, The longitudinal resistance of device D as a function of the bottom gate voltage (V_{bg}) in a range of V_{tg} at $T = 10\text{ K}$.

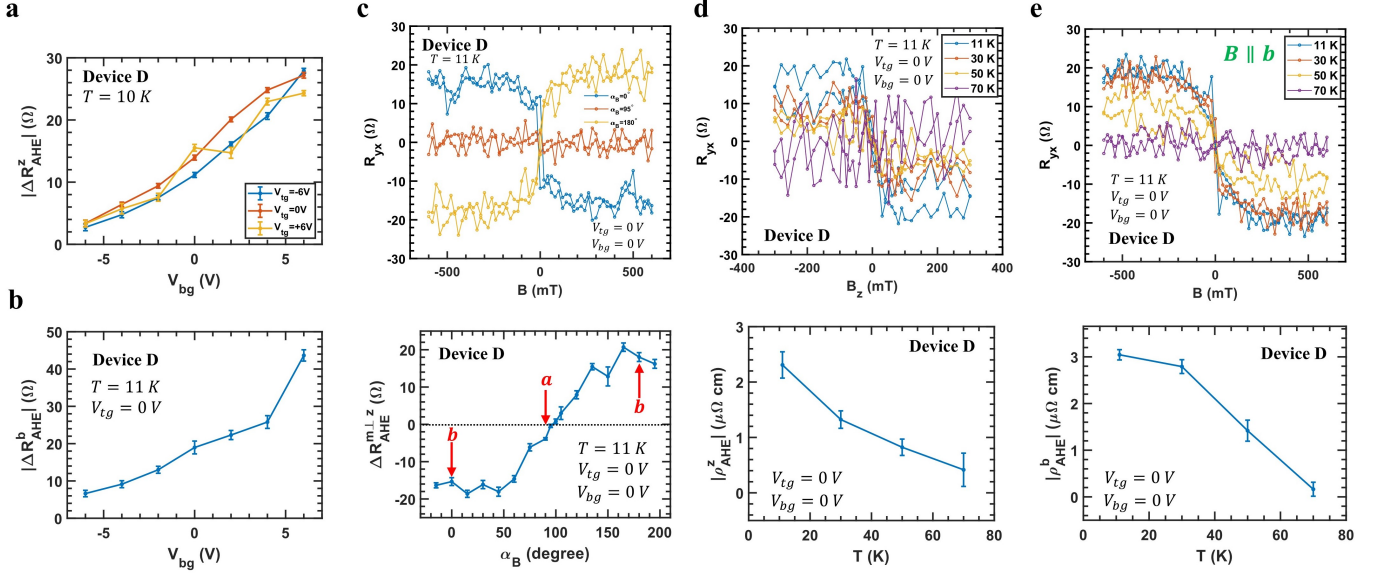


Fig. S7 Device D: Gate voltage, magnetic field angle, and temperature dependence results **a**, The m_z -dependent AHE resistance magnitude ($|\Delta R_{AHE}^z|$) in device D as a function of bottom gate voltage V_{bg} at various top gate voltage V_{tg} . **b**, The m_b -dependent AHE resistance magnitude ($|\Delta R_{AHE}^b|$) in device D as a function of bottom gate voltage V_{bg} . **c**, Upper panel: The R_{yx} vs B hysteresis loops measured in device D at various xy -plane rotation angle α_B . Lower panel: The in-plane AHE resistance ($\Delta R_{AHE}^{m,z}$) in device D as a function of α_B . **d**, Upper panel: The R_{yx} vs B_z hysteresis loops measured in device D at various temperatures. Lower panel: The m_z -dependent AHE resistivity magnitude ($|\rho_{AHE}^z|$) in device D as a function of temperature. **e**, Upper panel: The R_{yx} vs B ($B \parallel b$) hysteresis loops measured in device D at various temperatures. Lower panel: The m_b -dependent AHE resistivity magnitude ($|\rho_{AHE}^b|$) in device D as a function of temperature.

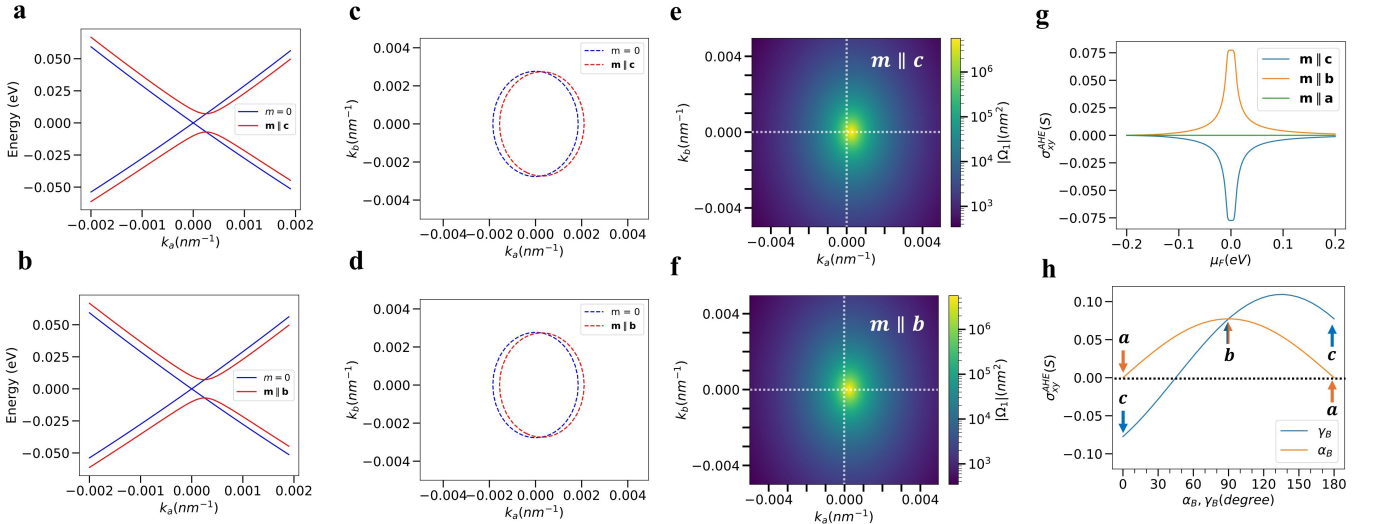


Fig. S8 Minimal microscopic model: Unconventional AHE in lower symmetry systems. **a,b**, Band structures for magnetization aligned along the c -axis (**a**) and along the b -axis (**b**) are shown with the band structure with no magnetization, using the following parameters: $g_{ab} = 20 \text{ eV} \cdot \text{nm}$, $g_{ba} = -20 \text{ eV} \cdot \text{nm}$, $g_{ac} = 20 \text{ eV} \cdot \text{nm}$, $\tilde{g}_{ac} = 10 \text{ eV} \cdot \text{nm}$, exchange coupling strength $\Delta_{ex} = 10 \text{ meV}$, and effective mass $\tilde{m}_a = \tilde{m}_b = 0.1m_e$. **c,d**, 2D band cut in k_a - k_b plane for $\mathbf{m} \parallel \mathbf{c}$ (**c**) and $\mathbf{m} \parallel \mathbf{b}$ (**d**). **e,f**, Berry curvature of the valence band for $\mathbf{m} \parallel \mathbf{c}$ (**e**) and $\mathbf{m} \parallel \mathbf{b}$ (**f**). **g**, The calculated anomalous Hall conductivity σ_{xy}^{AHE} as a function of electron chemical potential μ_F is shown for all three orthogonal magnetization configurations, qualitatively consistent with the experimental observations of AHE in a magnetic system with C_s symmetry. **h**, The calculated anomalous Hall conductivity σ_{xy}^{AHE} is shown as a function of the magnetic field angle when the field \mathbf{B} is rotated in the bc -plane (γ_B) and ab -plane (α_B), assuming the magnetization \mathbf{m} is aligned with the magnetic field ($\mathbf{m} \parallel \mathbf{B}$). The angle definitions are as follows: when $\gamma_B = 0^\circ$, $\mathbf{B} \parallel \mathbf{c}$; and when $\alpha_B = 0^\circ$, $\mathbf{B} \parallel \mathbf{a}$. The calculated results are consistent with the experimental observations of AHE in a magnetic system with C_s symmetry.